







ARTICLE

# Planar cell polarity induces local microtubule bundling for coordinated ciliary beating

Shogo Nakayama<sup>1,2</sup>, Tomoki Yano<sup>1,3</sup>, Toshinori Namba<sup>4</sup> , Satoshi Konishi<sup>1,5</sup> , Maki Takagishi<sup>6</sup>, Elisa Herawati<sup>7</sup> , Tomoki Nishida<sup>8</sup> , Yasuo Imoto<sup>8</sup>, Shuji Ishihara<sup>4</sup>, Masahide Takahashi<sup>9,10</sup> , Ken'ya Furuta<sup>11</sup>, Kazuhiro Oiwa<sup>11</sup>, Atsushi Tamura<sup>1,12,13</sup>, and Sachiko Tsukita<sup>1,13</sup> 

**Multiciliated cells (MCCs) in tracheas generate mucociliary clearance through coordinated ciliary beating. Apical microtubules (MTs) play a crucial role in this process by organizing the planar cell polarity (PCP)-dependent orientation of ciliary basal bodies (BBs), for which the underlying molecular basis remains elusive. Herein, we found that the deficiency of Daple, a dishevelled-associating protein, in tracheal MCCs impaired the planar polarized apical MTs without affecting the core PCP proteins, causing significant defects in the BB orientation at the cell level but not the tissue level. Using live-cell imaging and ultra-high voltage electron microscope tomography, we found that the apical MTs accumulated and were stabilized by side-by-side association with one side of the apical junctional complex, to which Daple was localized. In vitro binding and single-molecule imaging revealed that Daple directly bound to, bundled, and stabilized MTs through its dimerization. These features convey a PCP-related molecular basis for the polarization of apical MTs, which coordinate ciliary beating in tracheal MCCs.**

## Introduction

The apical differentiation of epithelial cells is critical for eliciting specific functions in biological systems. A single vertebrate epithelial multiciliated cell (MCC) bears hundreds of motile cilia that originate from basal bodies (BBs) located just beneath the apical membrane (Brooks and Wallingford, 2014; Spassky and Meunier, 2017; Roberson et al., 2020). The coordinated ciliary beating of MCCs generates directional fluid flow on the apical surface of the epithelia in the trachea, oviduct, and cerebral ventricle. Functional defects in this coordinated beating of cilia are associated with various diseases of the airways, reproductive tract, and brain (Dasgupta and Amack, 2016; Garcia and Reiter, 2016; Horani et al., 2016; Reiter and Leroux, 2017).

In the mammalian trachea, coordinated ciliary beating of MCCs is required for mucociliary clearance, which removes particles and pathogens as the first line of defense in the airways (Tilley et al., 2015; Bustamante-Marin and Ostrowski, 2017; Zapp and Morrisey, 2019). For efficient mucociliary clearance, the orientation of BBs is well coordinated by planar cell polarity (PCP) within individual MCCs (cell-level polarity) and between tracheal epithelial cells (tissue-level polarity; Boutin et al., 2014;

Butler and Wallingford, 2017; Spassky and Meunier, 2017). We previously found that, distinct from the orientation of BBs (the direction in which they face), the alignment of BBs (their spatial arrangement) was critical for the ordered distribution of BBs on the apical plane (Werner et al., 2011; Herawati et al., 2016). BB alignment is correlated with BB orientation, although the causal relationship is unclear.

Ciliary coordination in MCCs is established by PCP signaling pathways (Park et al., 2008; Guirao et al., 2010; Tissir et al., 2010; Ohata et al., 2014; Brooks and Wallingford, 2014; Shi et al., 2016; Butler and Wallingford, 2017; Lee et al., 2019). Core PCP proteins (i.e., integral membrane proteins, such as Frizzled [Fzd], Vangl, and cadherin EGF LAG seven-pass G-type receptor [Celsr]; and peripheral membrane proteins, such as Dishevelled [Dvl], Prickle [Pk], and Diego) and PCP effector proteins generate multiple cues to regulate the PCP-dependent architecture of MCCs for ciliary coordination at the cell and tissue levels (Vladar et al., 2009; Goodrich and Strutt, 2011; Boutin et al., 2014; Aw and Devenport, 2017; Butler and Wallingford, 2017; Davey and Moens, 2017).

<sup>1</sup>Laboratory of Barriology and Cell Biology, Graduate School of Frontier Biosciences, Osaka University, Osaka, Japan; <sup>2</sup>Integrative Physiology, Graduate School of Medicine, Osaka University, Osaka, Japan; <sup>3</sup>Department of Cardiovascular Medicine, Graduate School of Medicine, Osaka University, Osaka, Japan; <sup>4</sup>Department of Basic Science, Graduate School of Arts and Sciences, The University of Tokyo, Tokyo, Japan; <sup>5</sup>Department of Respiratory Medicine, Graduate School of Medicine, Kyoto University, Kyoto, Japan; <sup>6</sup>Department of Molecular Biosciences, University of Texas at Austin, Austin, TX; <sup>7</sup>Faculty of Mathematics and Natural Sciences, Universitas Sebelas Maret, Surakarta, Indonesia; <sup>8</sup>Japan Textile Products Quality and Technology Center, Hyogo, Japan; <sup>9</sup>Department of Pathology, Graduate School of Medicine, Nagoya University, Nagoya, Japan; <sup>10</sup>International Center for Cell and Gene Therapy, Fujita Health University, Toyoake, Japan; <sup>11</sup>Advanced Information and Communications Technology Research Institute, National Institute of Information and Communications Technology, Hyogo, Japan; <sup>12</sup>Department of Pharmacology, School of Medicine, Teikyo University, Tokyo, Japan; <sup>13</sup>Advanced Comprehensive Research Organization, Teikyo University, Tokyo, Japan.

Correspondence to Sachiko Tsukita: [atsukita@biosci.med.osaka-u.ac.jp](mailto:atsukita@biosci.med.osaka-u.ac.jp).

© 2021 Nakayama et al. This article is distributed under the terms of an Attribution–Noncommercial–Share Alike–No Mirror Sites license for the first six months after the publication date (see <http://www.rupress.org/terms/>). After six months it is available under a Creative Commons License (Attribution–Noncommercial–Share Alike 4.0 International license, as described at <https://creativecommons.org/licenses/by-nc-sa/4.0/>).

Among PCP-associated cues, the apical cytoskeleton, which is distributed in the apical plane, plays a unique role in MCCs, though the exact mechanism remains unclear. The basal foot (BF), as an appendage of the BB, interacts with the apical cytoskeleton, including the microtubules (MTs) and intermediate-sized filaments, to coordinate BB orientation and alignment in the apical plane just beneath the apical membranes of MCCs (Kunimoto et al., 2012; Vladar et al., 2012; Antoniadis et al., 2014; Garcia and Reiter, 2016; Herawati et al., 2016; Spassky and Meunier, 2017). In addition, the densities of MTs associated with cell membranes are higher on the Fzd side of the apical junctional complex (AJC) than on the Vangl side, and MT-depolymerizing nocodazole affects the coordination of BB orientation (Kunimoto et al., 2012; Vladar et al., 2012; Boutin et al., 2014; Herawati et al., 2016; Tateishi et al., 2017). Thus, planar polarized apical MTs play important roles in the coordination of BBs, the molecular mechanism of which is still unclear.

Daple, a Dvl-associated protein with a high frequency of leucine residues (Oshita et al., 2003; Siletti et al., 2017; Marivin et al., 2019; Marivin and Garcia-Marcos, 2019; Landin Malt et al., 2020), is involved in MT-dependent coordination of BB orientation. Daple-deficient ependymal cells display loss of the polarized distribution of apical MTs, inducing abnormal ependymal flow (Takagishi et al., 2017). However, the general molecular basis through which Daple coordinates the apical MT network has not yet been elucidated.

In this study, we evaluated the roles of Daple in mediating the PCP-dependent polarization of apical MTs. We also assessed the effects of Daple on the BB, focusing on analysis of BB orientation, not BB alignment. We found that deficiency of Daple in tracheal MCCs led to loss of PCP-dependent polarized apical MTs without influencing the localization of core PCP proteins. The tracheal MCCs of Daple-deficient mice induced abnormal polarity at the cellular level, with no severe polarity defects at the tissue level. To elucidate the unknown mechanisms underlying the organization of apical MTs through Daple in MCCs, we conducted *in vitro* analyses, including single-molecule analyses and cell-level analyses. Consequently, we showed that Daple organizes the polarized distribution of apical MTs by side-by-side association with the AJC and by MT bundling and stabilizing activities for ciliary coordination in MCCs.

## Results

### Daple is required for efficient airway mucociliary clearance by mediating coordination of BB orientation in tracheal MCCs

To analyze the functions of Daple, we first examined Daple localization in tracheal MCCs. In immunofluorescently labeled MCCs of WT and Daple-knockout (KO) tracheas and air-liquid interface (ALI) cultures of mouse tracheal epithelial cells (MTECs), we found no significant differences in the ratio of MCC number to total apical cell number (Fig. 1 A and Fig. S1, A-C). Immunofluorescent staining of MCCs showed that Daple localized specifically to the Fzd side of the AJC, which was marked by Fzd6 staining, but not to the Vangl side (Fig. S1, D and E).

To examine the role of Daple in mucociliary clearance in the trachea, we analyzed the fluid flow for mucociliary transport

using live imaging of fluorescent beads in WT, Daple-KO, and Vangl1-KO adult tracheas with active ciliary bending. The fluorescent beads uniformly flowed in a lung-to-mouth direction for mucociliary transport in the WT trachea (Fig. 1 B, Fig. S1 F, and Video 1). In contrast, the directional flow of fluorescent beads was modestly disrupted in Daple-KO, whereas the Vangl1-KO trachea exhibited severe defects in mucociliary transport (Fig. 1, B and C; Fig. S1 F; and Video 1), as shown by the ratio of the end-to-end distance to the distance along the bead trajectory (Fig. 1 C). These findings suggested that Daple deficiency moderately affected coordinated mucociliary transport in the trachea.

The efficiency of mucociliary transport depends on the bending direction of cilia, which is defined by the BB orientation. Hence, we examined the orientation of BBs using thin-section EM (TEM) in adult MCCs (Fig. 1, D and E). Daple-KO tracheal MCCs displayed moderate misorientation of BBs (Fig. 1, E and F). To follow the whole-cell orientation of BBs during development, we performed immunofluorescence microscopy and analyzed the positions of outer dense fiber 2 (Odf2; a BB marker) and centriolin/Cep128 (a BF marker; Fig. 1 D; Nakagawa et al., 2001; Gromley et al., 2003; Kashihara et al., 2019). Values for the index of orientation ( $I_o$ ), which indicates the degree of uniformity of the BB-BF orientation (Herawati et al., 2016), were similar between WT ( $0.44 \pm 0.04$ ) and Daple-KO ( $0.40 \pm 0.04$ ) tracheas at embryonic day 17.5 (E17.5; Fig. 1 G and Fig. S1 G). At postnatal day 2 (P2; early postnatal stage), the BB orientation was progressively more coordinated in WT tracheas ( $I_o$ ,  $0.69 \pm 0.02$ ), but not in Daple-KO tracheas ( $I_o$ ,  $0.44 \pm 0.04$ ). These differences persisted into the adult stage, although the absolute  $I_o$  values increased to  $0.91 \pm 0.02$  (WT) and  $0.78 \pm 0.06$  (Daple-KO; Fig. 1 G and Fig. S1 G). Hence, Daple may play critical roles in the coordination of BB orientation during development, particularly during the early MCC differentiation stage (E17.5 to P2 stages) of trachea development.

### Loss of Daple affects the coordination of BB orientation at the cell, but not tissue, level

Next we examined the tissue-level polarity in tracheal MCCs by analysis of the BB orientations of several MCCs (Fig. 2, A and B). The coordination of BB orientation at the cell level, as shown by the  $I_o$  value ( $I_o$  [Cell]), was similar to that at the tissue level ( $I_o$  [Tissue]) in WT and Daple-KO MCCs (Fig. 2 B; and Fig. S1, H and I), suggesting that tissue-level polarity was not affected by Daple-KO. In addition, there were no differences in the localization of core PCP proteins, such as Vangl1, Fzd6, and Prickle2, between WT and Daple-KO MCCs (Fig. 2, C-E; and Fig. S2, A-C).

In contrast, in the Vangl1-KO, the  $I_o$  (Tissue) value was lower than the  $I_o$  (Cell) value (Fig. 2 B), indicating that Vangl1 was critical for tissue-level coordination of BB orientation. There were two patterns of cellular distribution of Daple in Vangl1-KO tracheal MCCs (Fig. 2 F and Fig. S2 F). In one pattern (Vangl1-KO cell-1 in Fig. 2 F), Daple and Fzd6 displayed asymmetric localization within MCCs, although the direction of the asymmetry was random between cells (Fig. 2 F, left panel; and Fig. S2, D and E). In the other pattern (Vangl1-KO cell-2 in Fig. 2 F), Daple and Fzd6 no longer accumulated asymmetrically within the MCCs (Fig. 2 F, right panel; and Fig. S2, D and E). Therefore, in contrast

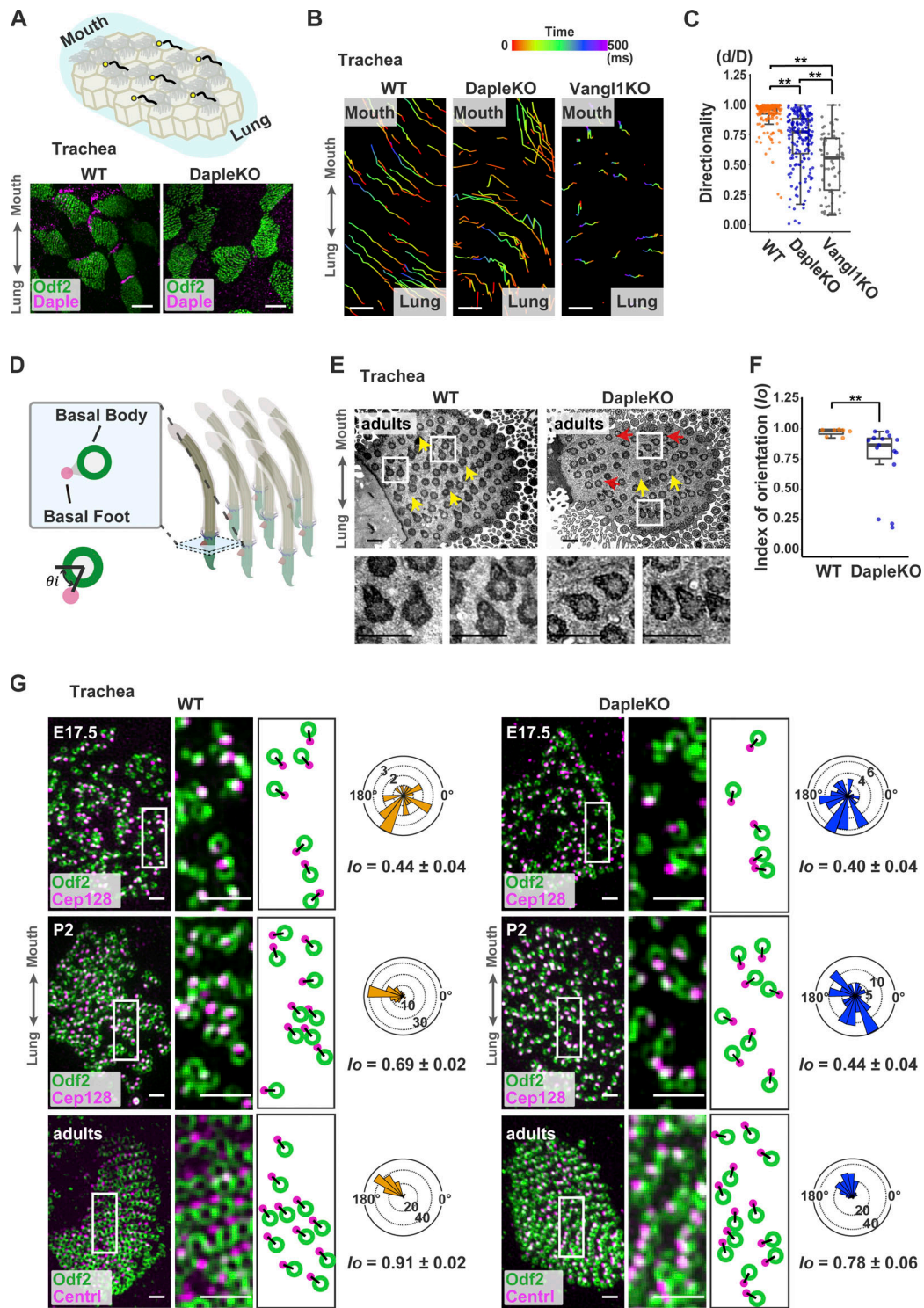


**Figure 1. Daple is required for coordinated ciliary beating in tracheal MCCs.** (A) Schematic illustration of mucociliary clearance on the tracheal surface (upper panel) and immunofluorescence images of Odf2 (green) and Daple (magenta) in the tracheas of WT and Daple-KO mice (lower panels). (B) Analyses of mucociliary transport in isolated WT, Daple-KO, and Vangl1-KO adult mouse tracheas using live imaging of fluorescent beads. The bead position at each time point is presented as a color corresponding to the time scale shown above the panel. Each bead was adjusted to a uniform starting time. Images are the magnified excerpts of boxes of micrographs shown in Fig. S1F. (C) The ratios of end-to-end distances ( $d$ ) against distances along the bead trajectory ( $D$ ) of the fluorescent beads in arbitrarily selected regions of isolated tracheal surfaces from WT ( $n = 182$ ), Daple-KO ( $n = 181$ ), and Vangl1-KO ( $n = 71$ ) mice. One-way ANOVA with Tukey-Kramer multiple-comparison test; \*\*,  $P < 0.01$ . (D) Schematic illustration of cilia structures. The ciliary bases contain the BB marked as a ring (green) and the BF as a dot (magenta). The angle  $\theta_i$  is between the horizontal axis and the vector originating from the center of the  $i$ th BB and ending at its BF. (E) Representative TEM images of WT and Daple-KO adult mouse tracheas. Yellow arrows indicate the direction of the BBs, and red arrows indicate abnormal orientation of BBs. High-magnification images of the boxed regions are shown in the lower panels. (F) Statistical analysis of the cell-level  $I_o$  of the BB orientation in WT ( $n = 7$  cells) and Daple-KO ( $n = 15$  cells) adult tracheas. Each data point represents all BBs involved in one cell. Two-tailed Mann-Whitney  $U$  test;

**\*\***,  $P < 0.01$ . **(G)** Representative immunofluorescence images of Odf2 and either centriolin or Cep128, respectively, with the BB marked as a ring (green) and the BF marked as a dot (magenta) in adult ( $n = 8$  cells), P2 ( $n = 13$  cells), and E17.5 ( $n = 10$ –12 cells) tracheas of WT and Daple-KO mice. High-magnification images of the boxed regions are shown with a line depicted from the center of the green ring to the center of the magenta dot and cell-level  $I_o$  indicating the BB orientation in MCCs. The double arrows indicate the directions of the mounted tracheas in A, B, E, and G. Scale bars represent 5  $\mu\text{m}$  in A, B, and G and 600 nm in E.

to the case of Vangl1 as a core PCP protein, the PCP effector protein Daple may function in the coordination of BB orientation at the cell level.

### Daple is essential for the polarized distribution of apical MTs to coordinate the BB orientation in MCCs

To elucidate how Daple regulates the orientation of BBs in tracheal MCCs, we examined the cytoskeleton in adult tracheas of WT and Daple-KO mice based on previous findings of differences in MT distribution in other organs (Takagishi et al., 2017). We used the ALI cultures of MTECs, owing to the clear visualization of the cytoskeleton in MCCs by super-resolution confocal immunofluorescence microscopy. We found almost no differences in the distribution patterns of intermediate-sized and actin filaments between WT and Daple-KO MCCs by immunofluorescence (Fig. S3, A–D). However, some differences were found for the MTs in MTECs (Fig. 3 A and Video 2). In WT MTECs, the apical MTs of MCCs showed a lattice-like arrangement at the apical plane just beneath the apical membrane, consistent with the results of the ultra-high voltage EM tomography (UHVEMT) in the trachea (Fig. 3 B). Apical MTs accumulated more at the Fzd side of the AJC, with gradually increasing intensities of MTs from the Vangl side to the Fzd side in mature MCCs of WT MTECs (Fig. 3, A and C), consistent with previous reports (Vladar et al., 2012). In contrast, the apical MTs in mature MCCs of Daple-KO MTECs did not accumulate on one side of the AJC, as confirmed by quantification of MT intensity (Fig. 3, C–F; and Fig. S3 E). UHVEMT of the WT trachea revealed that the planar polarized MTs were associated with the AJC on the Fzd side of an MCC and that MTs associated with the AJC by side-by-side association (Fig. 3 G and Video 3).

We next examined the effects of Vangl1 on the distribution of apical MTs. In Vangl1-KO MCCs of MTECs, two patterns of apical MT localization were detected. In one pattern, the apical MTs tended to accumulate on one side of the AJC, as shown in cell-1, in which Daple and Fzd6 displayed asymmetric localization (Fig. 4, A–D). These cells showed  $I_o$  values of BB orientation at the cell level similar to those of WT MCCs (Fig. 4, E–G). The apical MTs in the other pattern did not show one-side accumulation, as demonstrated for cell-2 (Fig. 4, A–D). In these cells, Fzd6 and Daple were not asymmetric (Fig. 4, A–D) and had lower  $I_o$  (Cell) values than those of WT MCCs for BB orientation (Fig. 4, E–G), suggesting impairment of the polarized distribution of apical MTs and of BB orientation in Vangl1-KO MTECs.

Analysis of co-cultured MTECs prepared from WT and Daple-KO tracheas (Fig. S3 F) showed that mature Daple-KO MCCs adjacent to WT MCCs did not display the asymmetric distribution of apical MTs (Fig. S3, G–I). These findings indicated that Daple acted in a cell-autonomous way to regulate the PCP-dependent polarized distribution of apical MTs.

### The Dvl- and $G\alpha_i$ -binding domains of Daple are dispensable for Daple-mediated MT organization activity

Daple has been reported to both trigger  $G\alpha_i$  protein activation through the  $G\alpha$  binding and activating (GBA) motif (Aznar et al., 2015; Leyme et al., 2017; Aznar et al., 2018; Marivin et al., 2019; Marivin and Garcia-Marcos, 2019; Marivin et al., 2020) and interact with Dvl and PARD3 through a PDZ-binding motif (PBM; Fig. 5 A; Oshita et al., 2003; Ishida-Takagishi et al., 2012; Ear et al., 2020). To investigate whether the GBA motif and PBM influence Daple-dependent accumulation and stabilization of apical MTs, we performed rescue analyses of Daple in Daple-KO MTECs using a lentivirus expression system. First, we confirmed that expression of the full-length (FL) monomeric enhanced GFP (mEGFP)-Daple (Daple FL) construct induced asymmetric localization to the Fzd side of AJC, similar to endogenous Daple in WT MCCs (Fig. 5 B), and concomitant accumulation of MTs to the mEGFP-Daple FL-positive AJC in Daple-KO MTECs (Fig. 5, C–E; and Fig. S4 F). When the polarized distributions of apical MTs were perturbed by weak nocodazole treatment, the asymmetric localizations of Daple and Fzd6 were not affected, suggesting that Daple localization did not depend on MTs (Fig. S4 A). Expression of the mEGFP-Daple GBA motif mutant (F1666A in the GBA motif of mouse Daple, which is the counterpart of F1675A in the GBA motif of human Daple; Aznar et al., 2018; Marivin et al., 2019; Fig. 5 A) in Daple-KO MTECs resulted in asymmetric localization to the Fzd side of the AJC (Fig. S4 B), along with the accumulation of MTs (Fig. S4, C–F). Unexpectedly, mEGFP-Daple lacking PBM ( $\Delta$ PBM) also colocalized with Fzd6 (Fig. 5 F) and induced the accumulation of MTs at the Fzd side of the AJC, where it was expressed (Fig. 5, G–I; and Fig. S4 F). These findings suggested that the  $G\alpha_i$  and Dvl interactive PBM domains of Daple were dispensable for the polarized association of MTs with the AJC at the Fzd side in tracheal MCCs (Fig. S4 G).

### Daple accumulates and immobilizes apical MTs around the Fzd side of the AJC

To investigate the mechanisms of PCP-dependent polarized organization of the apical MTs in tracheal MCCs, we performed live-cell imaging of EB1-mRuby3 (an MT plus-end binding protein) expressed by lentiviral infection in MTECs prepared from GFP-centrin2 transgenic WT mice (Fig. 6, A and B). As previously reported (Vladar et al., 2012), EB1 asymmetrically localized to the Fzd side of the AJC in tracheal MCCs (Fig. S5 A). Live-cell imaging revealed a difference in the EB1 resident time at the AJC between the Fzd and the other side in tracheal MCCs (Fig. 6, C and D; and Video 4). In WT MCCs, EB1 speed in the cytoplasm (interior [I]) was higher than that around the AJC (periphery [P]; Fig. 6 E and F), suggesting the presence of an interaction between MTs and the AJC. Importantly, EB1 speed at the Fzd side of

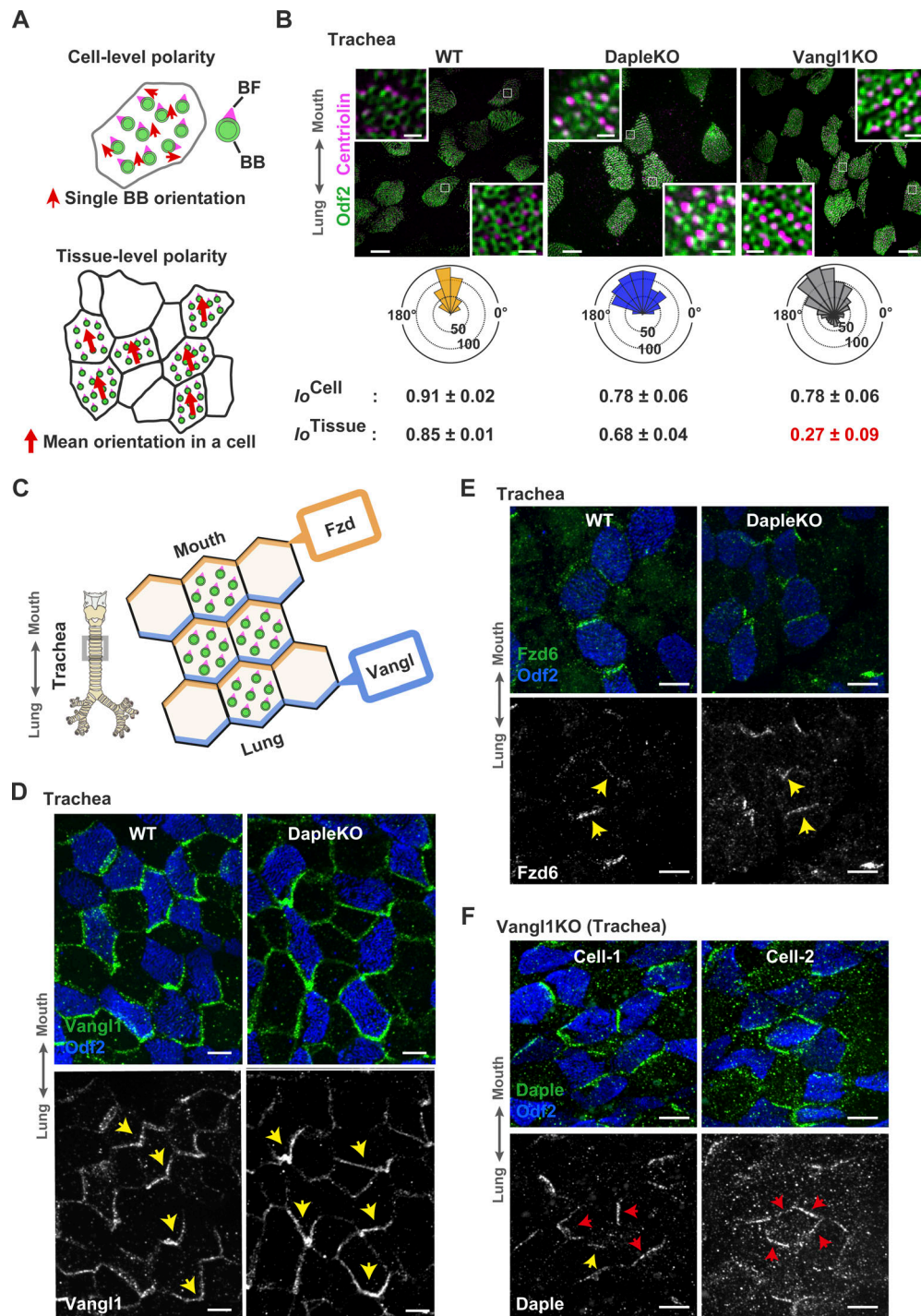
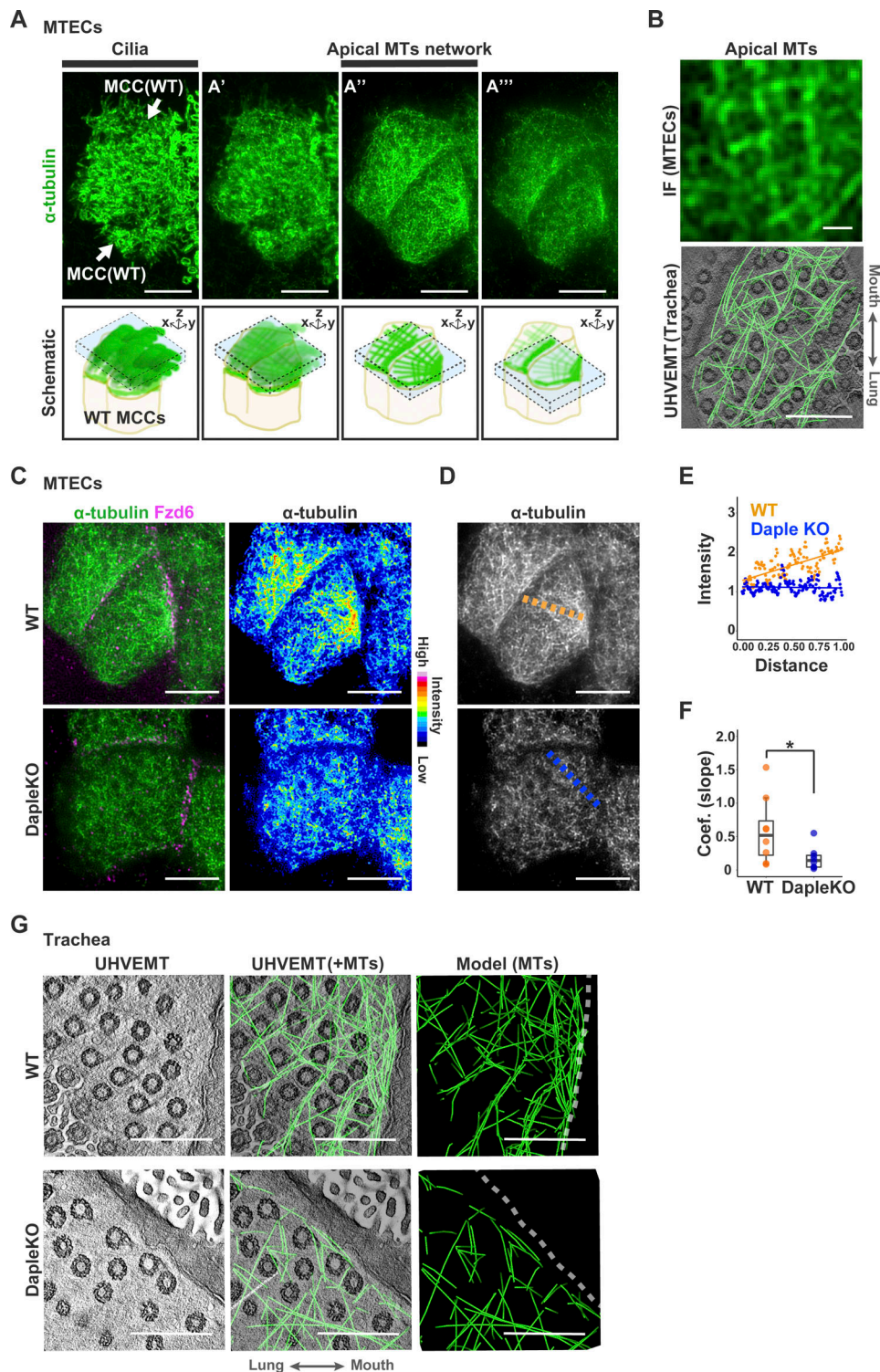
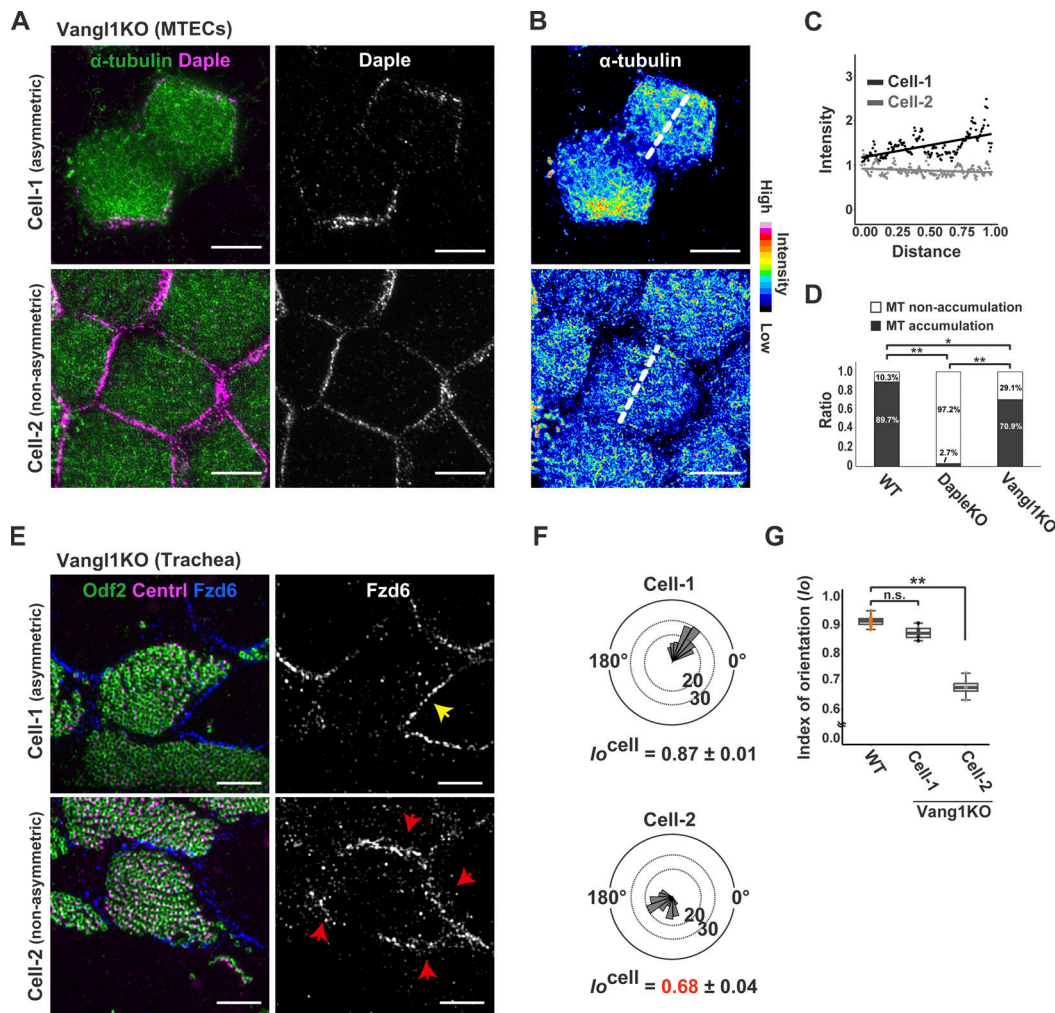


Figure 2. **Loss of Daple affects the cell-level polarity but does not largely affect the tissue-level polarity in the trachea.** (A) Schematic illustration of cell-level (arrow indicates the orientation of each BB in upper panel) and tissue-level (arrow indicates the combined orientations of BBs in a cell in lower panel) polarity. (B) Representative immunofluorescence images of Odf2 (green; BB) and centriolin (magenta; BF) in adult tracheas of WT, Daple-KO, and Vangl1-KO mice. Insets: High-magnification views of the boxed regions. Angle histograms of BB directions acquired from several MCCs in representative tracheas and the cell-level ( $n = 8$  cells) and tissue-level ( $n = 3$  tracheas) indices of orientation ( $Io$ ) are shown. (C) Schematic illustration of the localization of core PCP proteins (Fzd and Vangl) in the trachea. (D) Representative immunofluorescence images of Vangl1 (green) and Odf2 (blue) in adult tracheas of WT and Daple-KO mice. Yellow arrows indicate the localization of Vangl1 in tracheal MCCs. (E) Representative immunofluorescence images of Fzd6 (green) and Odf2 (blue) in adult tracheas of WT and Daple-KO mice. Yellow arrows indicate the localization of Fzd6 in tracheal MCCs. (F) Representative immunofluorescence images of Daple (green) and Odf2 (blue) in adult tracheas of Vangl1-KO mice. Yellow arrow indicates the localization of Daple at the Fzd side of the AJC, and red arrows indicate the abnormal localizations of Daple in tracheal MCCs. The double arrows indicate the directions of the mounted trachea in B–F. Scale bars represent 5  $\mu$ m (B, D–F) and 500 nm in insets in B, respectively.



**Figure 3. Establishment of planar polarized apical MTs requires Daple in tracheal MCCs.** **(A)** Representative super-resolution images of  $\alpha$ -tubulin as a marker of cilia and apical MTs in different z-slices (A', A'', and A''') in tracheal MCCs of WT MTECs grown on the ALI for 12–14 d, with illustrations showing z-slices in tracheal MCCs. Arrows display MCCs. **(B)** Comparison between a super-resolution fluorescence (IF) image for  $\alpha$ -tubulin (upper panels) and a UHVEMT image in which MTs are reconstituted in 3D (green; lower panels) in tracheal MCCs of isolated WT MTECs grown at the ALI for 12–14 d. **(C)** Immunofluorescence images of  $\alpha$ -tubulin and Fzd6 in WT and Daple-KO MTECs grown at the ALI for 12–14 d and color map of intensities of fluorescent signals for  $\alpha$ -tubulin in which red indicates high intensity and blue indicates low intensity. **(D and E)** Linear ROI setting (D) and intensity profiles along the ROI of immunofluorescence for  $\alpha$ -tubulin (E) in MCCs of WT (orange) and Daple-KO MTECs (blue). **(F)** Statistical analysis of the slope coefficient (Coef.) acquired from the intensity profiles (E) along the linear ROI setting in MCCs of WT (orange;  $n = 8$  cells) and Daple-KO MTECs (blue;  $n = 8$  cells). Two-tailed Mann-Whitney  $U$  test; \*,  $P < 0.05$ . **(G)** Representative UHVEMT images in which the MTs are reconstituted in 3D (green) in WT and Daple-KO adult tracheas. The dashed line shows the cell membrane. The double arrows indicate the direction of the mounted trachea in B and G. Scale bars represent 5  $\mu$ m in A, C, and D, and 500 nm in B and G.



**Figure 4. Role of Vangl1 in the formation of planar polarized apical MTs.** (A) Representative immunofluorescence images of  $\alpha$ -tubulin (green; a marker of apical MTs) and Daple (magenta) in MCCs of Vangl1-KO MTECs grown on the ALI for 12–14 d. (B) Color map of the signal for  $\alpha$ -tubulin corresponding to the images shown in A. (C) Intensity profiles of immunofluorescence for  $\alpha$ -tubulin in cell-1 (Fzd6 asymmetrical) and cell-2 (Fzd6 symmetrical) in tracheal MCCs of the Vangl1-KO. Intensity profiles were measured along linear ROIs (white) in B, which were drawn from the opposite side of the Fzd side of the AJC (distance, 0.00) to the Fzd6 side of the AJC (distance, 1.00) in cell-1 and arbitrarily between one side to the opposite side of the AJC in cell-2. (D) Ratios of the numbers of MCCs with MT accumulation (gray) to MT nonaccumulation (white) in the Fzd sides of the AJCs in WT, Daple-KO, and Vangl1-KO total MCCs ( $n = 39$ –55 cells). MCCs were visually divided into MT accumulation and MT nonaccumulation. Fisher’s exact test with the Benjamini-Hochberg multiple-comparison test; \*\*,  $P < 0.01$ ; \*,  $P < 0.05$ . (E) Representative images of triple-immunofluorescence for Odf2 (green) and centriolin (Centrl; magenta) as markers of BBs and BFs, respectively, and Fzd6 (blue) in Vangl1-KO adult tracheas. Yellow arrow indicates the asymmetrical localization of Fzd6. Red arrows indicate the abnormal localization of Fzd6 in MCCs. Note the asymmetrical localization of Fzd6 in cell-1 and the symmetrical localization of Fzd6 in cell-2 of Vangl1-KO MCCs. (F) Angle histograms of BB directions for representative cell-1 and cell-2 of Vangl1-KO tracheal MCCs corresponding to the images shown in E. Cell-level indices of orientation are in cell-1 ( $n = 4$  cells) and cell-2 ( $n = 4$  cells) of Vangl1-KO MCCs. (G) Boxplots of the indices of orientation in WT adult tracheal MCCs ( $n = 8$  cells), in cell-1 ( $n = 4$  cells), and in cell-2 ( $n = 4$  cells) of Vangl1-KO adult tracheal MCCs. Kruskal-Wallis tests with the Steel-Dwass multiple-comparison tests; \*\*,  $P < 0.01$ ; n.s.,  $P \geq 0.05$ . Scale bars represent 5  $\mu$ m.

the AJC, but not at the other side, was lower in WT MCCs (Fig. 6 G). When we observed EB1 dynamics at two sides (regions 1 and 2) of the AJC in Daple-KO MCCs, differences in EB1 dynamics between the sides of the AJC were not observed (Fig. S5, C and D; and Video 5). Moreover, the speed of EB1 movement in the cytoplasm (I) was also similar to that around the AJC (P; Fig. S5, E and F) in Daple-KO MCCs. These results suggested that Daple restricted EB1 dynamics at the Fzd side of the AJC (Fig. 6 H).

Next, we performed live-cell imaging of MTs using MTECs expressing mEGFP- $\alpha$ -tubulin. The GFP signal was significantly

stronger in the cilia and apical regions of the MCCs (Fig. S5 G). Kymograph analysis showed that the dynamics of apical MTs was decreased at the Fzd side of the AJC in WT MTECs (Fig. 6 I). When we compared the dynamics of MTs in WT and Daple-KO MCCs, the dynamics at the Fzd side of the AJC were significantly lower than those at the other side in WT MCCs (Fig. 6, J and K; and Video 6). Conversely, Daple-KO MCCs did not show these effects in the dynamics of MTs at the AJC (Fig. 6 J and Video 6). These results suggested that the lateral interaction of MTs with the AJC at the Fzd side in a side-by-side manner was stabilized directly or indirectly by Daple in tracheal MCCs.

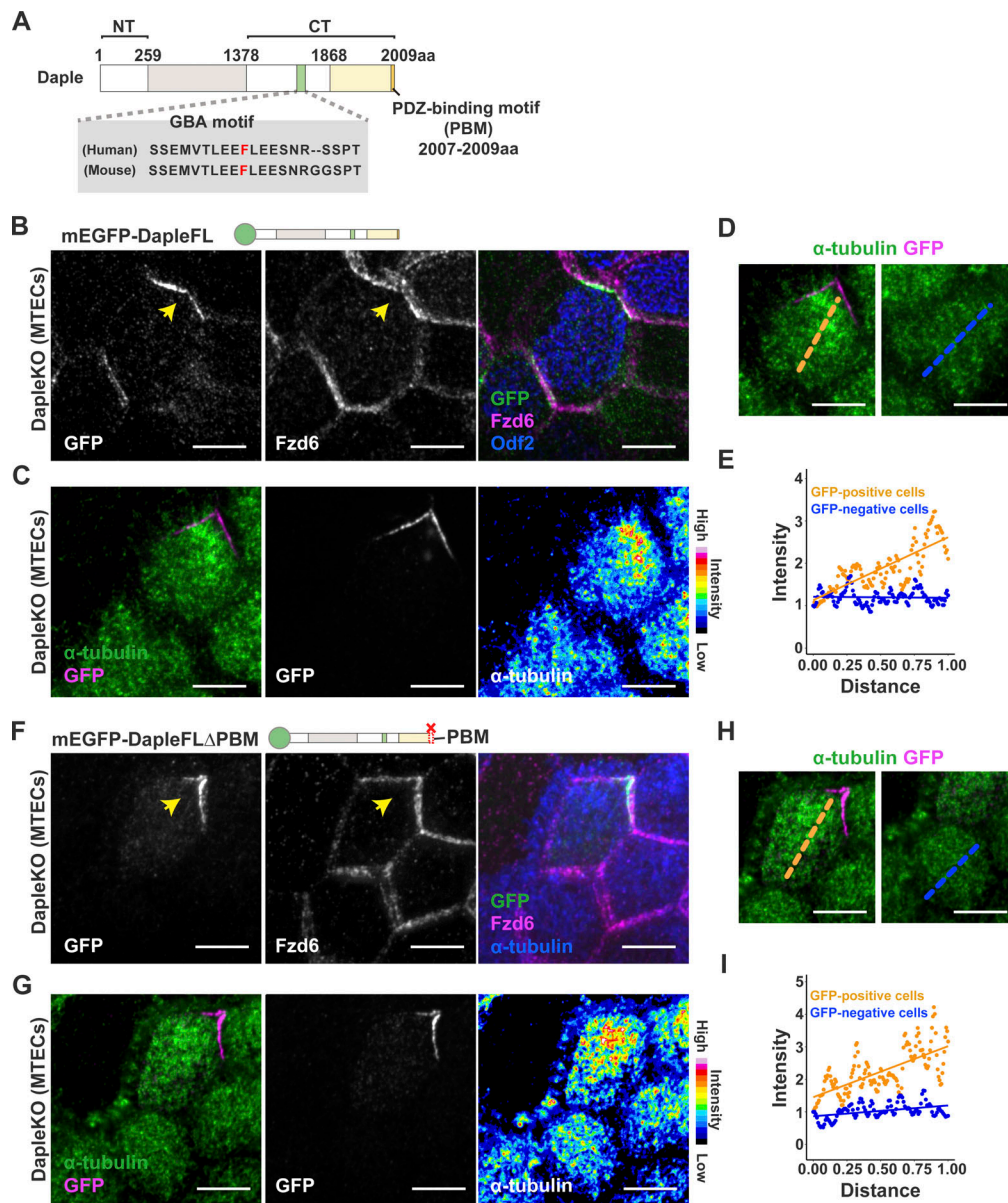


**Figure 5. The Dvl interactive domain, PBM, of Daple is not required for Daple-mediated apical MT organization.** (A) Schematic drawing of Daple FL and its GBA motif and PBM. A comparison between the mouse and human Daple amino acid sequences is shown. (B) Representative immunofluorescence images of mEGFP–Daple FL (green), Fzd6 (magenta), and Odf2 (blue; a marker of MCCs) in Daple-KO MTECs expressing mEGFP–Daple FL. mEGFP–Daple FL was expressed using the lentivirus system. Arrows indicate mEGFP–Daple FL and Fzd6 localization in tracheal MCCs. (C) Representative immunofluorescence images of mEGFP–Daple FL (magenta) and  $\alpha$ -tubulin (green) in Daple-KO MTECs expressing mEGFP–Daple FL. The intensity of the fluorescence signal for  $\alpha$ -tubulin is represented by the color map, where red indicates high intensity and blue indicates low intensity. (D and E) Intensity profiles of  $\alpha$ -tubulin along the linear ROI in mEGFP–Daple FL-positive MCCs (orange) and GFP-negative MCCs (blue) in Daple-KO MTECs. The linear ROI was drawn from the opposite side of the Fzd side of the AJC (distance, 0.00) to the Fzd6 side of the AJC (distance, 1.00). (F) Representative immunofluorescence images of mEGFP–Daple FL  $\Delta$ PBM (green), Fzd6 (magenta), and  $\alpha$ -tubulin (blue) in Daple-KO MTECs, in which mEGFP–Daple FL  $\Delta$ PBM was expressed. Arrows indicate localization of mEGFP–Daple FL  $\Delta$ PBM and  $\alpha$ -tubulin in tracheal MCCs. (G) Representative images of mEGFP–Daple FL  $\Delta$ PBM (magenta) and  $\alpha$ -tubulin (green) in Daple-KO MTECs expressing mEGFP–Daple FL  $\Delta$ PBM. The intensity of the fluorescence signal for  $\alpha$ -tubulin is represented by the color map, where red indicates high intensity and blue indicates low intensity. (H and I) Intensity profiles of  $\alpha$ -tubulin along the linear ROI in mEGFP–Daple FL  $\Delta$ PBM-positive MCCs (orange) and GFP-negative MCCs (blue) in Daple-KO MTECs. The linear ROI was drawn from the opposite side of the Fzd side of the AJC (distance, 0.00) to the Fzd6 side of the AJC (distance, 1.00). Scale bars represent 5  $\mu$ m.

**Daple directly interacts with MTs via its C-terminal (CT) region**

Next, we examined the interaction of Daple with MTs in detail. A coimmunoprecipitation (co-IP) assay using HEK293T cells showed the association of Daple with MTs (Fig. 7 A). To further examine the direct association, we performed an MT co-

sedimentation assay using Daple FL protein purified from HEK293T cells. The results showed that Daple FL directly bound to MTs ( $K_d = 1.46 \mu$ M; Fig. 7 B). Additionally, MT co-sedimentation assays of the Daple CT domain (Daple CT), Daple N-terminal domain (Daple NT), and Daple lacking CT (Daple



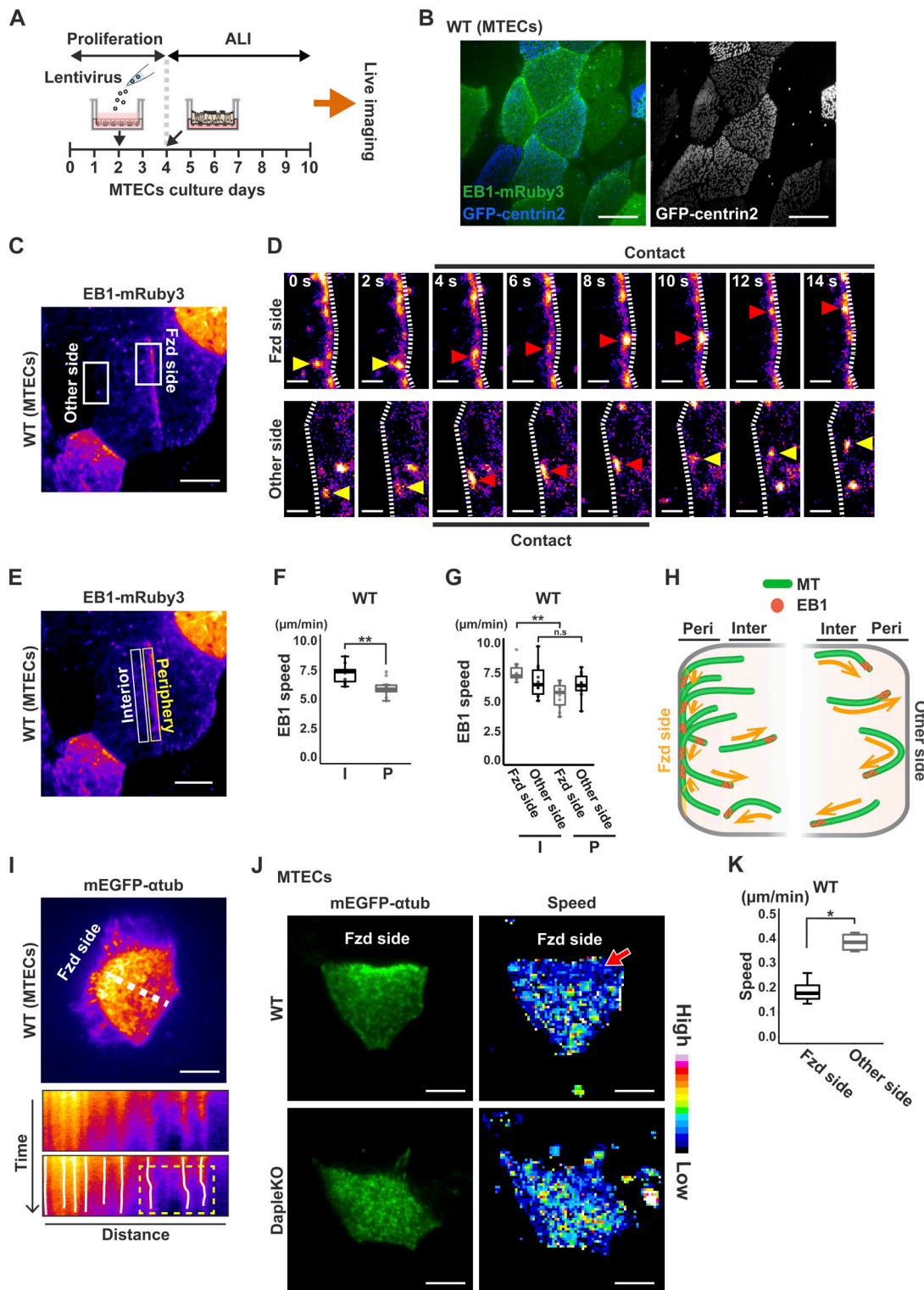


**Figure 6. Daple regulates MT dynamics at the Fzd side of the AJC in tracheal MCCs.** (A) Schematic drawing of ALI culture of MTECs for the lentivirus infection and live imaging. (B) Representative fluorescence images of EB1-mRuby3 (green) and centrin2 (blue) in GFP-centrin2-positive WT MTECs expressing EB1-mRuby3 via the lentivirus system. (C and D) Representative image for EB1-mRuby3 (red) in GFP-centrin2-positive WT MTECs expressing EB1-mRuby3 due to the lentivirus system (C) and time-lapse images of the boxed regions in C for EB1-mRuby3 at the Fzd and the other side of the AJC in tracheal MCCs (D). Red arrows indicate the EB1 comets that contact the cell membrane, whereas yellow arrows indicate the EB1 comets in the cytoplasm. (E) Representative fluorescence image for EB1-mRuby3 in GFP-centrin2-positive WT MTECs with boxes indicating the I and P regions. (F) EB1 speed at the I and P regions in MCCs of WT MTECs. Speed of EB1 comets showing spatial differences ( $n = 10$ ). Two-tailed Mann-Whitney  $U$  test; \*\*,  $P < 0.01$ . (G) EB1 speeds in the I and P regions around the Fzd and the other sides of the AJC in MCCs of WT MTECs ( $n = 10$  cells). Kruskal-Wallis test with the Steel-Dwass multiple-comparison test; \*\*,  $P < 0.01$ ; n.s.,  $P \geq 0.05$ . (H) Schematic illustration of differences in EB1 dynamics around the Fzd and other side of the AJC in MCCs of GFP-centrin2-positive WT

MTECs. The EB1 comets display a long residence time at the Fzd side of the AJC. Inter, I region; Peri, P region. **(i)** Representative image for mEGFP- $\alpha$ -tubulin (mEGFP- $\alpha$ -tub; red) expressed in MCCs of WT MTECs (upper panel) and kymograph showing the motility of MTs in MCCs of WT MTECs (lower panel). Note the high motility of MTs as they move near the Vangl side of the AJC, as shown in the boxed region (yellow dashed lines). **(j)** Representative images of mEGFP- $\alpha$ -tubulin in MCCs of WT and Daple-KO MTECs (left panels) and analyses of MT live imaging using the LPX flow plugin (right panels). The movement speed of the  $\alpha$ -tubulin signal is represented by colors (red indicates high speed; blue indicates low speed). The arrow indicates a decrease in speed at the Fzd side of the AJC in WT MCCs. **(k)** Statistical analysis of the speed of MTs in WT MCCs ( $n = 4$  cells). ROIs were set at the Fzd and other side of the AJC. Two-tailed Mann-Whitney U test; \*,  $P < 0.05$ . Scale bars represent 5  $\mu\text{m}$  in B, C, E, I, and J and 1  $\mu\text{m}$  in D.

$\Delta$ CT) showed that Daple CT, but not Daple NT and  $\Delta$ CT, directly bound to MTs (Fig. 7 C). We then expressed the mEGFP-Daple CT  $\Delta$ Fzd-binding domain (aa 1868–2009; Aznar et al., 2015, 2018) in WT MTECs. The mEGFP-Daple CT  $\Delta$ Fzd-binding domain showed cytosolic localization and did not localize to the Fzd side of the AJC, whereas mEGFP-Daple CT localized to the Fzd side of the AJC in MCCs (Fig. 7 D). Next, we performed domain analyses on Daple CT, which was divided into two separate peptides, aa 1390–1867 and 1868–2009, of the CT regions (Fig. 7 E). Daple 1390–1867 bound to MTs, similar to Daple CT, as shown by co-IP assays (Fig. 7 E). Consistent with this, anti- $\alpha$ -tubulin immunostaining did not show an asymmetric distribution of apical MTs in Daple-KO MCCs expressing the Daple FL  $\Delta$ 1390–1867 domain (Fig. 7, F and G; and Fig. S5 H). Hence, Daple CT may be responsible for MT accumulation on the Fzd side of the AJC. However, when mEGFP-Daple CT was expressed in Daple-KO MTECs, MT accumulation did not occur on any side of the AJC, despite localization of mEGFP-Daple CT on the Fzd side of the AJC (Fig. 7, H and I). Thus, recruitment of the MT-binding domain (CT 1390–1867) to the Fzd side of the AJC by the Fzd-binding domain of Daple was not sufficient for the asymmetric distribution of MTs at the Fzd side of the AJC in MCCs. Further studies are needed to assess the roles of the Daple NT and coiled-coil domain in the polarized organization of apical MTs.

### The NT domain of Daple is essential for the asymmetric association of apical MTs with the AJC in tracheal MCCs

Next, we examined the association of Daple with MTs using live imaging via total internal reflection fluorescence (TIRF) microscopy (Fig. 8 A). ATTO 647N-labeled MTs were immobilized on a cover glass, and mEGFP-Daple FL protein and its domains purified from HEK293T cells were added (Fig. 8, A–D; and Video 7). The results showed that Daple FL and Daple CT laterally bound to MTs (Fig. 8, B–F), whereas Daple NT and Daple  $\Delta$ CT did not bind to MTs (Fig. 8, E and F), confirming that Daple bound laterally to MTs via its CT domain.

Because the expression of mEGFP-Daple CT did not induce the asymmetric distribution of apical MTs when transfected into MCCs of MTECs (Fig. 7, H and I), we hypothesized that another region of Daple (NT and coiled-coil domain) may be required for the polarized organization of MTs in tracheal MCCs. Importantly, UHVEMT suggested that planar polarized MTs, likely bundled, were associated with the AJC in a side-by-side manner on the Fzd side of MCCs in WT but not Daple-KO MCCs (Fig. 9 A and Video 8). MT bundling proteins, such as MAP65, cross-link MTs through their dimerization (Subramanian et al., 2010; Burkart and Dixit, 2019; Bodakuntla et al., 2019). Therefore, we examined the possibility of oligomerization of Daple by imaging the fluorescent spots of a single mEGFP-Daple molecule on a

glass surface (Yukawa et al., 2019). Most spots of Daple FL,  $\Delta$ CT, and NT displayed a two-step photobleaching behavior (Fig. 9 B), whereas most spots of Daple CT showed photobleaching in less than two steps (Fig. 9 B). We then quantified the intensities of mEGFP-Daple spots. The intensity profile of Daple FL was more similar to those of  $\Delta$ CT and NT than that of CT, supporting the dimerization of Daple FL,  $\Delta$ CT, and NT (Fig. 9 C). Collectively, these results suggested that Daple FL dimerized through the NT region.

To evaluate the effects of Daple dimerization on MTs, mEGFP-Daple FL or Daple CT was mixed with ATTO 647N-labeled MTs, and the mixture was placed on a glass coverslip (Fig. 9 D). MTs associated with Daple FL showed a higher signal intensity than MTs alone (Fig. 9 E), suggesting the bundling of MTs by Daple FL. By contrast, MTs associated with Daple CT showed almost the same signal intensity as MTs alone on a glass surface (Fig. 9 E). Next, negative staining EM showed that Daple FL, but not Daple CT, bundled MTs (Fig. 9 F). Taken together, these findings suggested that the polarized organization of apical MTs required the MT bundling activity of Daple (Fig. 9 G and Fig. 10).

## Discussion

Various signaling pathways modulate PCP-dependent cellular processes, which are critical for morphogenesis (Boutin et al., 2014; Devenport, 2014; Chien et al., 2015; Yang and Mlodzik, 2015; Butler and Wallingford, 2017; Fuertes-Alvarez et al., 2018; Haag et al., 2018; Singh et al., 2018). Although PCP was first thought to represent tissue polarity, pioneering studies in the *Drosophila* wing and vertebrate inner ear have shed light on the role of the polarized organization of apical cytoskeletons, particularly actin filaments and MTs, in establishing PCP for the polarized arrangement of actin hairs, stereocilia, and kinocilia in an evolutionarily conserved manner (Steyger et al., 1989; Eaton, 1997; Strutt et al., 1997; Mlodzik, 2020). Further studies revealed the links between core PCP proteins and regulatory proteins of actin filaments, such as Rho-family proteins or their binding proteins in various PCP-mediated contexts (Boutros et al., 1998; Winter et al., 2001; Habas et al., 2001). More recently, the roles of apical MTs and/or actin filaments in PCP processes have attracted attention in relation to cilia and centrosome positioning (Wallingford, 2010; Carvajal-Gonzalez et al., 2016a, 2016b; Dasgupta and Amack, 2016). These functions are distinct from the roles of cytoplasmic MTs, which regulate core PCP protein trafficking (Shimada et al., 2006). However, the detailed molecular mechanisms of the apical cytoskeleton in PCP-related, multifaceted events remain elusive.

MT-associated proteins, such as MAP7, CLAMP, and dynein, also have roles in PCP-related cell polarization (Sipe et al., 2013;

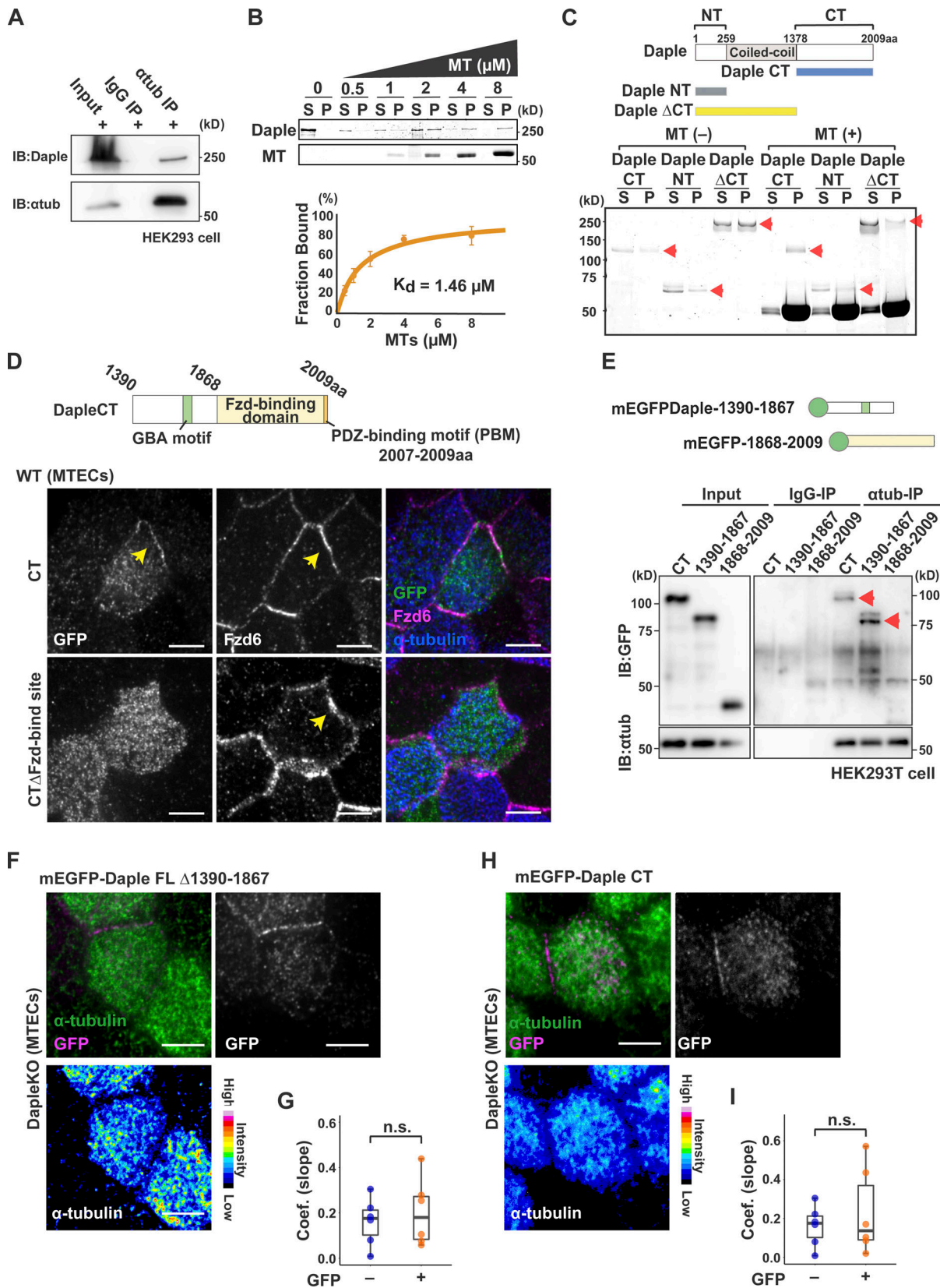


Figure 7. **Daple directly interacted with apical MTs to show planar polarization.** (A) Co-IP of Daple with  $\alpha$ -tubulin (atub). mEGFP–Daple FL was exogenously overexpressed in HEK293T cells and pulled down using an anti- $\alpha$ -tubulin antibody. IB, immunoblotting. (B) MT co-sedimentation assay with purified mEGFP–Daple FL protein. Coomassie Blue–stained SDS–PAGE gels showing the binding behavior of 500 nM mEGFP–Daple FL in the presence of increasing concentrations of MTs (upper panel). Results from three experiments were plotted and fit to a Michaelis–Menten equation ( $K_d \pm$  SD,  $1.46 \pm 0.187 \mu\text{M}$  for Daple

FL; lower panel). S, supernatant; P, pellet. **(C)** MT co-sedimentation assay with purified mEGFP–Daple CT and NT domains and mEGFP–Daple FL  $\Delta$ CT. Schematic illustration of Daple CT and NT domains and Daple  $\Delta$ CT (upper panel). Coomassie Blue–stained SDS–PAGE gels (lower panel) showing the binding behavior of mEGFP–Daple CT (750 nM), mEGFP–Daple NT (1.2  $\mu$ M), and mEGFP–Daple  $\Delta$ CT (480 nM) with 10  $\mu$ M MTs. Red arrows show Daple and its indicated domains. **(D)** Schematic illustration of the Daple CT domain (upper panel) and representative images of WT MTECs expressing mEGFP–Daple CT and the CT domain lacking Fzd-binding domain (1868–2006 aa; CT  $\Delta$ Fzd-binding domain) via a lentivirus system (lower panel). mEGFP (green), Fzd6 (magenta), and  $\alpha$ -tubulin (blue). Arrows indicate the asymmetrical localization of Fzd6 and CT at the AJC. **(E)** Co-IP of the mEGFP–Daple 1390–1867 or 1868–2009 domains with  $\alpha$ -tubulin. mEGFP–Daple domains were exogenously overexpressed in HEK293T cells and pulled down with an anti- $\alpha$ -tubulin antibody. Red arrows show Daple and its indicated domains. **(F)** Representative immunofluorescence images of mEGFP–Daple FL  $\Delta$ 1390–1867 (magenta) and  $\alpha$ -tubulin (green) in Daple-KO MTECs expressing mEGFP–Daple FL  $\Delta$ 1390–1867 via a lentivirus system. The intensity of the  $\alpha$ -tubulin signal is represented by the color map (red indicates high intensity; blue indicates low intensity). **(G)** Statistical analyses of the slope coefficients (Coef.) acquired from the intensity profiles of the immunofluorescence for  $\alpha$ -tubulin along the linear ROI set either from the opposite to the Fzd6 side of the AJC in mEGFP-positive MCCs (orange) or arbitrarily between one side and the opposite side of the AJC in mEGFP-negative MCCs (blue) of Daple-KO MTECs expressing mEGFP–Daple FL  $\Delta$ 1390–1867 via a lentivirus system ( $n = 6$  cells). Two-tailed Mann-Whitney  $U$  test; n.s.,  $P \geq 0.05$ . **(H)** Representative immunofluorescence images of Daple-KO MTECs expressing the mEGFP–Daple CT domain via a lentivirus system for signals of mEGFP (magenta) and  $\alpha$ -tubulin (green). The intensity of the  $\alpha$ -tubulin signal is represented by the color map (red indicates high intensity; blue indicates low intensity). **(I)** Statistical analyses of the slope coefficients acquired from the intensity profiles of the immunofluorescence intensities for  $\alpha$ -tubulin along the linear ROI set either from the opposite side of the Fzd side of the AJC to the Fzd6 side of the AJC in mEGFP-positive MCCs (orange) or arbitrarily between one side and the opposite side of the AJC in mEGFP-negative MCCs (blue) of Daple-KO MTECs expressing the mEGFP–Daple CT domain via a lentivirus system ( $n = 6$  cells). Two-tailed Mann-Whitney  $U$  test; n.s.,  $P \geq 0.05$ . Scale bars represent 5  $\mu$ m.

Kim et al., 2018; Landin Malt et al., 2019; Takagishi et al., 2020). Dvl regulates MT dynamics through interactions with MAPs (Krylova et al., 2000; Ciani et al., 2004; Kikuchi et al., 2018). Herein, we showed that the Daple FL  $\Delta$ PBM domain, which did not interact with Dvl, colocalized with Fzd6 and induced the accumulation of MTs at the Fzd side of the AJC. In contrast, although Daple CT localized to the Fzd side of the AJC, the Daple CT  $\Delta$ Fzd-binding domain, which lacked interactions with Fzd, displayed cytoplasmic localization in tracheal MCCs. Hence, in tracheal MCCs, the asymmetric localization of Daple is dependent on Fzd and is required but not sufficient for the asymmetric distribution of apical MTs. However, whether MT regulation through Dvl and other factors may work collaboratively with the Daple–MT system remains unclear. Interestingly, Daple anchors cytoplasmic dynein to generate a pulling force on MTs connected to BBs in ependymal cells (Takagishi et al., 2020). In the current study, we confirmed that the direct binding activity of Daple with MTs was required for asymmetric MT accumulation in tracheal MCCs. Further studies are required to determine whether dynein may work collaboratively with direct Daple–MT interactions in tracheal MCCs.

One of the most prominent characteristics of the cytoskeleton is its association with specific areas of the plasma membrane. Two patterns of association are recognized (i.e., end-on or lateral side-by-side associations), in which the end or the side of cytoskeletal filaments are associated with a specific membrane area (Yano et al., 2013; Toya and Takeichi, 2016; Yano et al., 2017, 2018; Bodakuntla et al., 2019; Tsukita et al., 2019a, 2019b, 2020; Yano et al., 2021). In this study, we showed that tracheal MCCs in Daple-deficient mice displayed loss of PCP-dependent apical MTs and abnormal BB orientation at the cell level. We demonstrated the side-by-side association of apical MTs with the Fzd side of the AJC and showed that MT bundling and stabilization by Daple played important roles in the asymmetric distribution of apical MTs. Thus, Daple, as an Fzd- and Dvl-associated protein, organized the asymmetric distribution of apical MTs to coordinate the ciliary beating in MCCs for efficient mucociliary transport in the trachea as a primary barrier to infection.

Our *in vitro* assays showed that Daple directly bound to MTs via its CT domain and dimerized via its NT domain to bundle MTs. At the cellular level, the MT filaments were largely stabilized at the Fzd side of the AJC in tracheal MCCs. In addition, MTs were laterally associated with the AJC in a side-by-side manner at the Fzd–Daple side, and the prominently higher density of apical MTs was associated with the Fzd–Daple side compared with the opposite Vangl side. Moreover, at the organ level, *in vivo* live imaging demonstrated disruption of mucociliary transport in Daple-KO and Vangl1-KO tracheas. Finally, although Daple was essential for the PCP-dependent asymmetric distribution of apical MTs in MCCs, it was not critical for coordination of BB orientation at the tissue level, in contrast to Vangl1, a core PCP protein.

Notably, we found that loss of PCP-dependent apical MTs owing to lack of Daple led to a significantly lower  $I_0$  value in adult tracheal MCCs. This change in BB orientation caused by loss of Daple expression in adult MCCs was milder than that stimulated by nocodazole treatment, which induced random BB orientations (Herawati et al., 2016). During development, the absolute  $I_0$  values were increased in Daple-KO MCCs. Based on this finding, Daple-independent MTs, which are sensitive to nocodazole, may be important for coordinating ciliary beating to some extent. Indeed, apical MTs connecting BBs remain visible in Daple-KO MCCs. In addition, previous studies identified intermediate-sized filaments directly beneath the apical membrane in tracheal MCCs. Apical intermediate-sized filaments start to form networks around P2–P4, whereas apical MTs form at E17.5 in tracheal MCCs (Tateishi et al., 2017). This spatio-temporal organization of apical cytoskeletons in tracheal MCCs may establish sophisticated functions, such as BB orientation and alignment.

Based on our findings, the MT network may organize coordinated ciliary beating via a multistep process. MCCs contain both Daple-dependent and -independent apical MTs, which are sensitive to nocodazole. Daple-independent MTs are involved in the basic architectural development of apical MTs, whereas Daple-dependent MTs may be required for the robust coordination of BB orientation. Thus, the mechanism of Daple-mediated

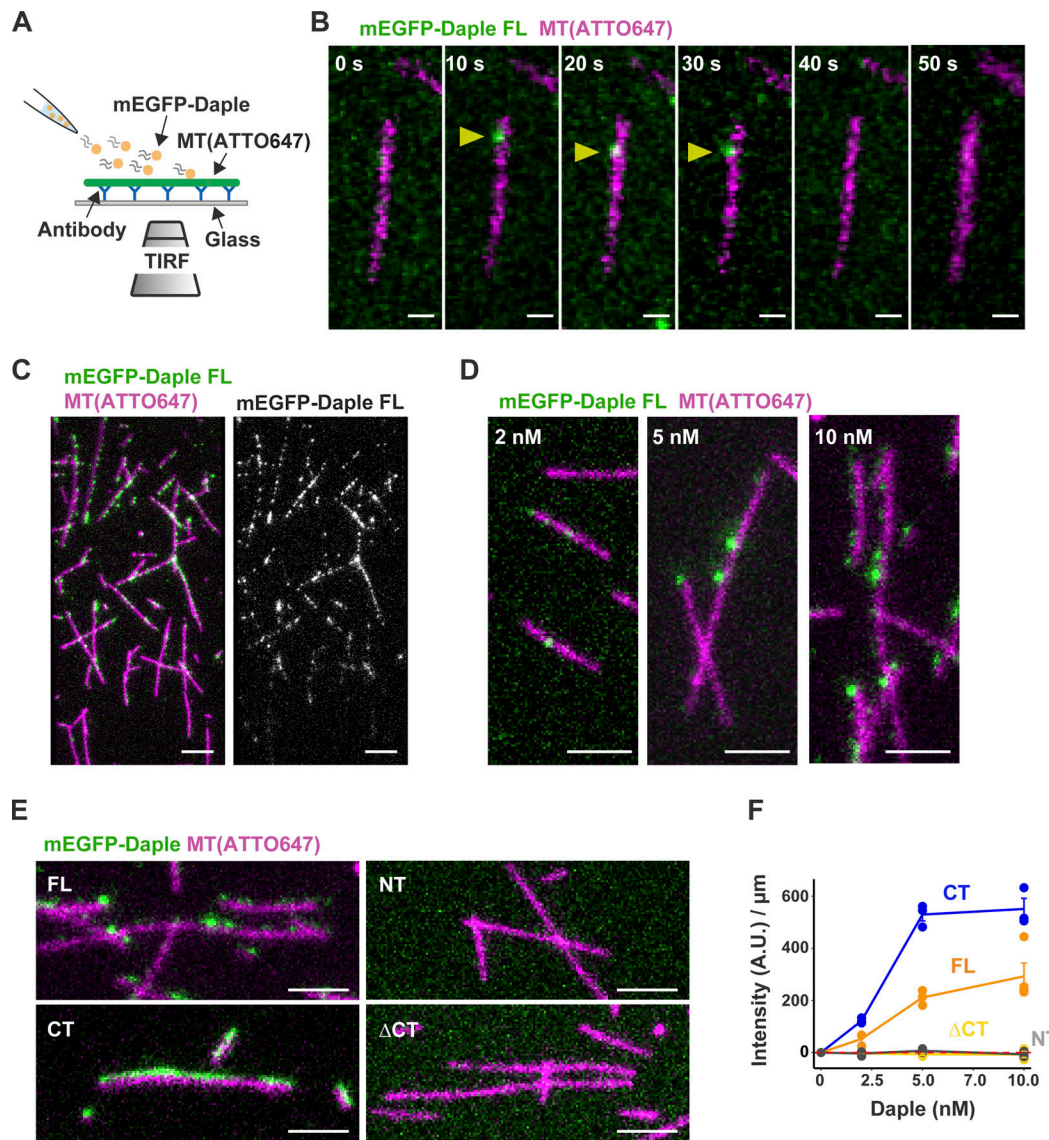


**Figure 8. Single-molecule behavior of Daple along MTs.** (A) Schematic illustration of live imaging of single Daple molecules along an immobilized MT using TIRF microscopy. (B) Time-lapse images of the single-molecule assay with 2 nM mEGFP-Daple FL (green) with fluorescently labeled MTs (magenta). Arrowheads indicate mEGFP-Daple FL molecules. (C) Single frame of the single-molecule assay with 10 nM mEGFP-Daple FL (green) with fluorescently labeled MTs (magenta). (D) Single frames of the single-molecule assays with different concentrations (2, 5, and 10 nM) of mEGFP-Daple FL (green) with fluorescently labeled MTs (magenta). (E) Single frames of the single-molecule assays with 10 μM mEGFP-Daple FL, CT, NT, and ΔCT (green) with fluorescently labeled MTs (magenta). (F) Signal intensity of mEGFP-Daple FL, CT, NT, and ΔCT molecules along an MT ( $n = 15$ ). Lines represent the mean signal intensity with SE. Scale bars represent 5 μm. A.U., arbitrary units.

BB coordination may be at least partly explained by the hydrodynamic model of BB alignment. In this model, the apical cytoskeleton acts as a viscoelastic fluid, providing a self-organizing mechanism to align and orient BBs coordinately for mucociliary transport in tracheal MCCs (Herawati et al., 2016; Namba and Ishihara, 2020). However, the detailed mechanisms underlying Daple-dependent and -independent MT coordination and BB orientation remain unclear.

In the current study, Vangl1-KO showed variable phenotypes with respect to BB orientation. In Vangl1-KO MCCs, in which Daple showed an asymmetric distribution in the AJC, the apical MTs also showed planar polarization. Moreover, in some of the Vangl1-KO MCCs in which Daple did not show an asymmetric

distribution in the AJC, apical MTs were not polarized, confirming the specific role of Daple in generating the asymmetric MT distribution. In addition, in Vangl1-KO MCCs, coordination of BB orientation was impaired at the tissue level, unlike in Daple-KO MCCs. These results were consistent with the roles of apical MTs in BB coordination at the cellular level (Vladar et al., 2012; Boutin et al., 2014). Additionally, our results suggested that the Daple-dependent asymmetric apical MT distribution likely did not play an important role in the tissue-level polarity of BB orientation. Thus, our findings revealed the specific role of Daple, a PCP effector protein, in organizing the specific stage of cell-level polarity downstream of PCP core proteins.

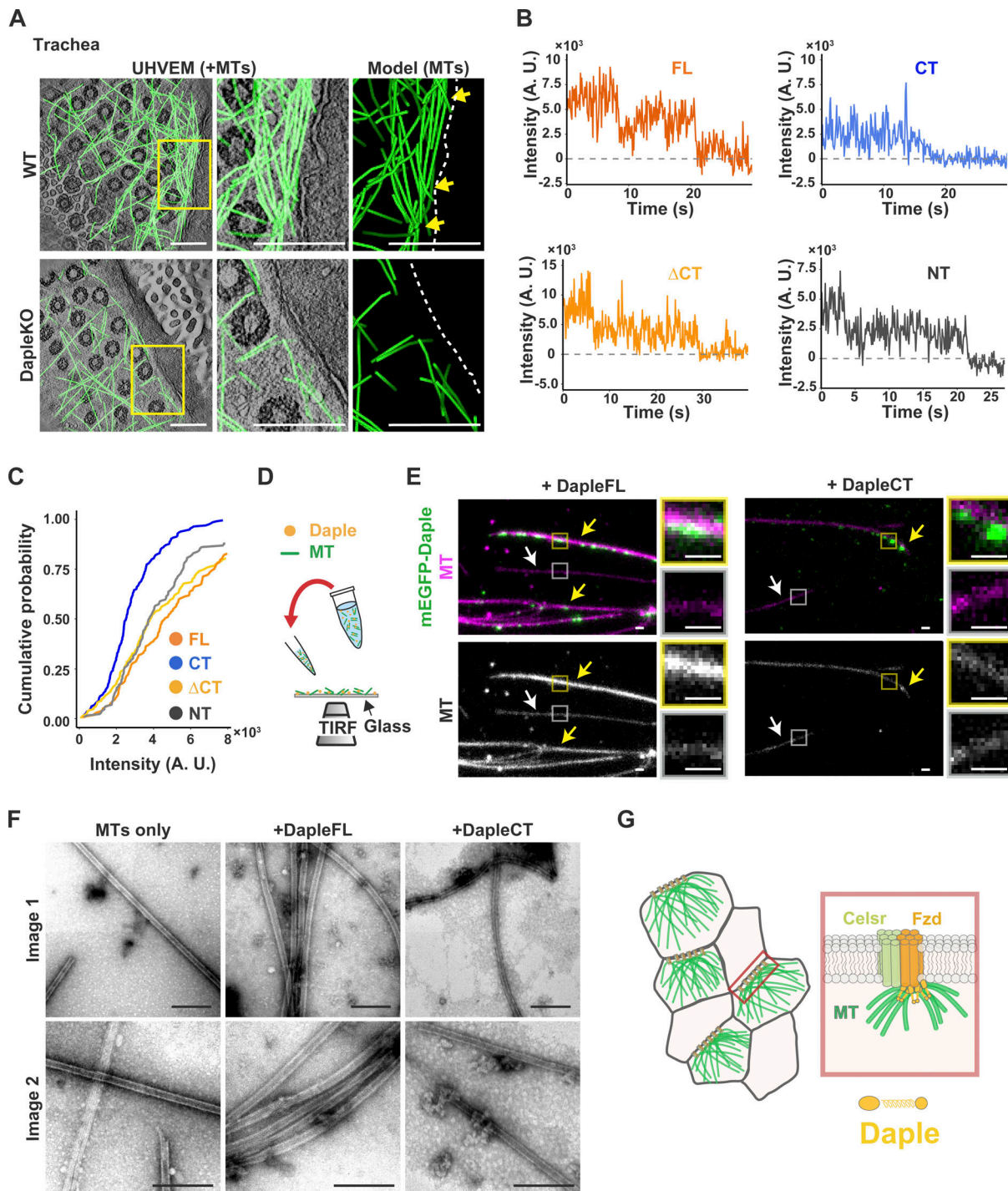


**Figure 9. Planar polarized MTs are organized by Daple through MT bundling.** (A) Representative images of the reconstituted UHVEMT with an extracted model of MTs (green) in WT and Daple-KO mouse tracheas (left; shown in Fig. 3 G), and magnification for the yellow boxed regions of either both models (middle) or only the extracted model of MTs (right). Arrows indicate apical MTs bundled at the Fzd side of the AJC. (B) Stepwise bleaching of spots of mEGFP-Daple FL, CT, NT, and ΔCT molecules. (C) Cumulative histogram of initial fluorescence intensities of immobilized spots of mEGFP-Daple FL ( $n = 158$ ), mEGFP-Daple CT ( $n = 196$ ), mEGFP-Daple ΔCT ( $n = 213$ ), and mEGFP-Daple NT ( $n = 129$ ). (D) Schematic illustration of the MT bundling assay. The mixture of Daple and MTs was added to the flow chamber. Samples were imaged using TIRF microscopy. (E) Representative TIRF images of the MT bundling assay with mEGFP-Daple FL (or CT; green) and fluorescently labeled MTs (magenta). Yellow arrows indicate MTs to which Daple bound, and white arrows indicate MTs to which Daple did not bind. High-magnification images of the boxed regions are shown. (F) Representative images of negative staining EM of MTs alone (left panel), MTs with 10 μM Daple FL (middle panel), or MTs with 10 μM Daple CT (right panel). (G) Schematic drawing of the interaction between Daple and MTs at the Fzd side of the AJC. Daple directly binds to, bundles, and stabilizes MTs through its dimerization and accumulates apical MTs at the Fzd side of AJC in MCCs. Scale bars represent 250 nm in A, 1 μm in E, and 200 nm in F. A.U., arbitrary units.

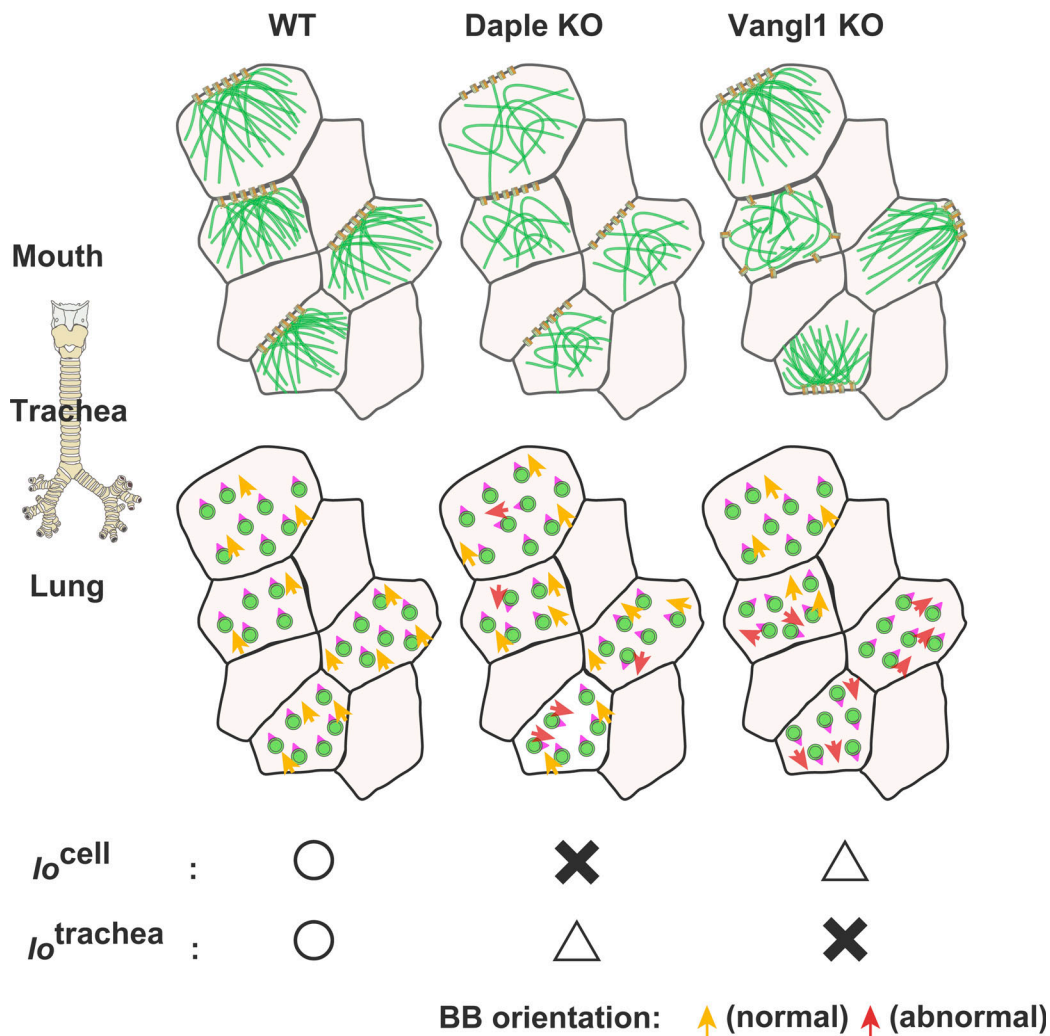


Figure 10. **Daple-dependent apical MTs organize coordinated ciliary beating.** Schematic illustration of the phenotype of Daple-KO and Vangl1-KO MCCs. Daple KO in tracheal MCCs impair planar polarized apical MTs and induce significant defects in BB orientation at the cell level but not at the tissue level, whereas Vangl1-KO MCCs display significant defects in BB orientation at the tissue level. In Vangl1-KO MCCs, two patterns of apical MT localization were detected. In one pattern, the apical MTs tended to accumulate on one side of the AJC, whereas the other pattern did not show one-sided accumulation.

The apical maturation of epithelial cells is essential for epithelial functions, in which the role of the cytoskeleton is notable; for example, the roles of actin filaments in intestinal microvilli and cochlear stereocilia and the roles of MTs in cilia in primary ciliary cells or MCCs (Hudspeth, 2014; Bayless et al., 2016; Dasgupta and Amack, 2016; Bustamante-Marin and Ostrowski, 2017; Soh et al., 2020). Herein, we demonstrated the PCP-dependent multistep apical maturation of tracheal MCCs, in which core PCP and PCP effector proteins were cooperatively and/or sequentially functionalized for coordinated ciliary beating for efficient mucociliary transport. Daple is a PCP effector protein associated with the core PCP proteins Fzd and Dvl and plays a critical role in the asymmetric distribution of apical MTs at the Fzd side of the AJC. Vangl1 is a PCP core protein that is associated with Pk and may function in the coordination of asymmetrically distributed apical MTs at the cell and tissue levels upstream of PCP effector proteins. Thus, the step-by-step analyses of PCP-dependent maturation of epithelial cells will lead to a comprehensive understanding of the functional

differentiation of epithelial cells in general. In this respect, MCCs could provide a typical example in which apical maturation leads to coordinated ciliary beating for mucociliary transport as a primary barrier against infection.

## Materials and methods

### Antibodies

The following primary antibodies were used in this study: rabbit anti-Odf2 polyclonal antibody (pAb; 1:1,000 for immunofluorescence; ab43840; Abcam), rat anti-Odf2 mAb (1:1,000 for immunofluorescence; Tateishi et al., 2013), rabbit anti-Daple (1:500 for immunofluorescence and Western blotting; 28147; IBL), rat anti-centriolin mAb generated previously (undiluted for immunofluorescence; Ishikawa et al., 2005), rabbit anti-Cep128 mAb generated previously (1:500 for immunofluorescence; Kashihara et al., 2019), goat anti-Fzd6 pAb (1:250 for immunofluorescence; AF1526; R&D Systems), rabbit anti-Vangl1 pAb (1:500 for immunofluorescence; HPA025235; Sigma-Aldrich),

rabbit anti-ZO1 pAb (1:500 for immunofluorescence; catalog no. 617300; Life Technologies), rabbit anti-Prickle2 pAb (1:500 for immunofluorescence; a kind gift from Dr. T. Otsuka, University of Yamaguchi, Yamaguchi, Japan), rabbit anti- $\alpha$ -tubulin (1:1,000 for Western blotting; 11224-1-AP; Proteintech), mouse anti- $\alpha$ -tubulin mAb (1:1,000 for immunofluorescence; 1:10 for IP; T9026; Sigma-Aldrich), rat anti-keratin8 mAb (undiluted for immunofluorescence; [Tateishi et al., 2017](#)), rat anti-tyrosinated tubulin mAb (1:500 for immunofluorescence; ab6160; Abcam), mouse anti-GFP mAb (1:10 for IP; A11120; Life Technologies), rabbit anti-GFP pAb (1:500 for Western blotting; A-6455; Invitrogen), and rat anti-GFP mAb (1:500 for immunofluorescence; 04404-26; Nacalai Tesque). The secondary antibodies used in this study were as follows: donkey anti-rabbit IgG (H+L) Alexa Fluor 488 (A21206; Invitrogen), donkey anti-rabbit IgG (H+L) Alexa Fluor 568 (10042; Invitrogen), donkey anti-rabbit IgG (H+L) Alexa Fluor 647 (A-31573; Invitrogen), donkey anti-rat IgG (H+L) Alexa Fluor 488 (A-21208; Invitrogen), goat anti-rat IgG (H+L) Alexa Fluor 568 (A-11077; Invitrogen), goat anti-rat IgG (H+L) Alexa Fluor 647 (A-21247; Invitrogen), donkey anti-mouse IgG (H+L) Alexa Fluor 488 (A-21202; Invitrogen), donkey anti-mouse IgG (H+L) Alexa Fluor 568 (A-10037; Invitrogen), donkey anti-mouse IgG (H+L) Alexa Fluor 647 (A-31571; Invitrogen), donkey anti-goat IgG (H+L) Alexa Fluor 488 (A-11055; Invitrogen), donkey anti-goat IgG (H+L) Alexa Fluor 568 (A-11057; Invitrogen), donkey anti-goat IgG (H+L) Alexa Fluor 647 (A-21447; Invitrogen), goat anti-rabbit IgG (H+L) HRP conjugate (NA934V; GE Healthcare), goat anti-rat IgG (H+L) HRP conjugate (NA935V; GE Healthcare), and goat anti-mouse IgG (H+L) HRP conjugate (NA931V; GE Healthcare). For actin staining, we used rhodamine-conjugated phalloidin (1:1,000; R415; Invitrogen).

### Animals

All procedures involving animals were approved by the Osaka University Institutional Animal Care and Use Committee (FBS-17-005). Daple-KO mice were obtained from the trans-National Institutes of Health Knockout Mouse Program Repository (University of California, Davis, Davis, CA; [Skarnes et al., 2011](#)) and have been described previously ([Takagishi et al., 2017](#)). GFP-centrin2 transgenic mice ([Higginbotham et al., 2004](#)) and Vangl1-KO mice ([Song et al., 2010](#)) were used in this study. To generate Daple-KO-expressing GFP-centrin2 mice, homozygous GFP-centrin2 mice were crossed with homozygous Daple-KO mice. Homozygous Daple-KO GFP-centrin2 mice were obtained by heterozygous mating.

### Primary culture of tracheal cells

MTEC cultures were prepared from the trachea of mice at 8–20 wk of age ([You et al., 2002](#); [Herawati et al., 2016](#)). To improve the cell yield, enzymatic digestion was performed with gentle shaking at 4°C for 18 h and terminated by adding FBS (172012; Sigma-Aldrich) to the cell suspension at a final concentration of 10%. Cells were pooled by centrifugation at 400  $\times$  g at 4°C for 10 min and then resuspended in MTEC Basic Medium ([You et al., 2002](#); [Herawati et al., 2016](#)) with 10% FBS at 37°C for 3.5 h and 5% CO<sub>2</sub> to allow contaminating fibroblasts to adhere to the flask. Nonadherent cells were then collected by centrifugation and

seeded onto polyester Transwell 24-well filters (3470; Corning) coated with 50  $\mu$ g/ml collagen type I (354249; Corning). The proliferation stage was maintained using a commercially available BEGM BulletKit (CC-3170; Lonza). The ALI condition was created after 4 d of culture using PneumaCult (05001; STEMCELL Technologies) according to the manufacturer's instructions.

### Cell culture

HEK293T cells ([Graham et al., 1977](#)) were used for experiments with cultured cells. Cells were cultured in DMEM (05919; Nissui Pharmaceutical) supplemented with 10% FBS (172012; Sigma-Aldrich) and 0.45% wt/vol glucose solution (079-05511; Wako) at 37°C in an atmosphere containing 5% CO<sub>2</sub>.

### Immunofluorescence

MTECs and whole-mount tracheas were fixed in cold methanol for 10 min at -20°C or in 4% paraformaldehyde in Hepes-buffered saline (HBS) at room temperature (rt) for 7 min, permeabilized with 0.2% Triton X-100/PBS at rt for 5 min, and then incubated in 1% BSA/PBS at rt for 30 min. Incubations with primary and secondary antibodies were performed at 24  $\pm$  3°C for 1 h each, as previously described ([Herawati et al., 2016](#); [Tateishi et al., 2017](#)). Samples were observed using spinning-disk Olympus super-resolution microscopy (Olympus) and disk scanning unit (DSU) microscopy (Olympus). Images were obtained using a silicon oil immersion objective lens (UPlanSApo 60 $\times$ S; NA 1.30; working distance [WD], 0.30 mm; Olympus), an oil immersion objective lens (UPlanFLN 40 $\times$ O; NA 1.30; WD, 0.20 mm; Olympus) or PlanApoN 60 $\times$ O; NA 1.42; WD, 0.15 mm; Olympus), a dry objective lens (UPlanSApo 20 $\times$ ; NA 0.75; WD, 0.60 mm; Olympus), a 1.6 $\times$  conversion lens with either a scientific complementary metal-oxide-semiconductor (sCMOS) camera (ORCA-Flash 4.0 v2; Hamamatsu Photonics) or a charge-coupled device (CCD) camera (ORCA-R2; Hamamatsu Photonics). The microscope system was equipped with appropriate filter sets for DAPI/FITC/TRITC, a motorized scanning deck, and an incubation chamber (37°C, 5% CO<sub>2</sub>, 85% humidity; Tokai Hit). Image acquisition was set to a z-series of 6–30 planes with a 0.25- $\mu$ m distance. Hardware was controlled using MetaMorph software (Molecular Devices). The resulting 3D images were converted into 2D images by maximum-intensity projection in the z-direction before image analysis.

### Purification of mEGFP(A206K)-Daple-Flag using HEK293T cells

Daple FL, Daple CT, Daple NT, and Daple  $\Delta$ CT were amplified using PCR from a mouse brain cDNA library and inserted into the pEGFP-C1-Flag vector, which was constructed by the insertion of a Flag-tag into the pEGFP-C1 vector (6084-1; Clontech). We then modified EGFP to mEGFP with an A206K mutation to obtain the mEGFP-Daple plasmids. HEK293T cells in 10-cm dishes were transfected with 6  $\mu$ g mEGFP-Daple-Flag plasmids using PEI MAX (Polysciences) according to the manufacturer's instructions. Cells were washed three times with ice-cold HBS and then scraped with 200  $\mu$ l lysis buffer (250 mM NaCl, 10% sucrose, 1 mM MgSO<sub>4</sub>, 20 mM Hepes, pH 7.5, and a protease inhibitor cocktail [03969; Nacalai Tesque]). The resuspended



cells were then disrupted using a sonicator and centrifuged at  $20,400 \times g$  at  $4^\circ\text{C}$  for 30 min. The supernatant was incubated with 20  $\mu\text{l}$  anti-Flag M2 affinity gel beads (A2220; Sigma-Aldrich) at  $4^\circ\text{C}$  for 18 h. Following incubation, the beads were washed four times with ice-cold HBS and then eluted with the 3X-FLAG peptide (F4799; Sigma-Aldrich) in ice-cold HBS containing the protease inhibitor cocktail (03969; Nacalai Tesque) and 1 mM DTT (Y00147; Invitrogen) following the manufacturer's instructions.

### Lentivirus plasmids and production

EGFP-Daple FL, EGFP-Daple CT, EGFP-Daple GBA motif mutant, EGFP-Daple  $\Delta\text{PBM}$ , EGFP-Daple 1390-1867, EGFP-Daple 1868-2009, EGFP-Daple  $\Delta\text{1390-1867}$ , and EGFP- $\alpha$ -tubulin were constructed by ligating PCR-amplified Daple FL, Daple CT, Daple GBA motif mutant, Daple  $\Delta\text{PBM}$ , Daple 1390-1867, Daple 1868-2009, Daple  $\Delta\text{1390-1867}$ , and  $\alpha$ -tubulin into the pEGFP-C1 vector (6084-1; Clontech). EGFP-Daple FL, EGFP-Daple CT, EGFP-Daple GBA, EGFP-Daple  $\Delta\text{PBM}$ , EGFP-Daple 1390-1867, EGFP-Daple 1868-2009, EGFP-Daple  $\Delta\text{1390-1867}$ , and EGFP- $\alpha$ -tubulin were inserted into the pLV5IN-CMV Neo vector (6181; Takara). We then modified EGFP to mEGFP with an A206K mutation to obtain the mEGFP plasmids. The Daple GBA motif mutant was obtained by modification of F1666A by mutagenesis. Mouse EBI was amplified using PCR and inserted into the pNCS-mRuby3 vector (a kind gift from Dr. Michael Z. Lin, Stanford University, Stanford, CA; [Bajar et al., 2016](#)). EBI-mRuby3 was amplified using PCR and was inserted into the pLV5IN-CMV Neo vector (6181; Takara) to obtain pLV5IN-EBI-mRuby3 plasmids. Recombinant lentivirus was produced by transient cotransfection of HEK293T cells with Lentiviral High Titer Packaging Mix (6149; Takara) using the PEI MAX transfection reagent (24765-1; Polysciences). The lentiviral supernatant was harvested 48 h after transfection and filtered through a  $0.45\text{-}\mu\text{m}$  PES filter (SLHPO33NK; Merck Millipore). The lentiviral supernatants were mixed with polyethylene glycol 6000 (169-09125; Wako) and incubated at  $4^\circ\text{C}$  for 18 h. Following incubation, the mixture was concentrated 100-500-fold by centrifugation at  $5,000 \times g$  at  $4^\circ\text{C}$  for 30 min.

### Lentiviral infection

For the lentiviral infection of MTECs, the medium was removed, and cells were rinsed with PBS. To allow virus access to the basolateral surface, MTECs were infected at the proliferation stage. Fresh medium was added to the bottom of the dish, and a mixture of lentivirus and medium was placed on top of the cells. The virus was removed ~24-48 h after infection. Cells were used for the assay after ALI culture for 7-8 d.

### Live imaging of MTECs

The live imaging of MTECs was performed as previously described ([Herawati et al., 2016](#)). Transwell filters with an MTEC sheet (ALI 7-8 d) were cut out from the plastic support and inverted (cell side facing down) onto a glass-bottomed dish (D11140H; Matsunami Glass). The medium was supplied from an additional chamber attached to the back surface of the inverted insert. Samples were observed using a spinning-disk Olympus

super-resolution microscope (Olympus) and a DSU microscope (Olympus). Images were obtained using a silicon oil immersion objective lens (UPlanSApo 60 $\times$ S; NA 1.30; WD, 0.30 mm; Olympus), a 1.6 $\times$  conversion lens with either an sCMOS camera (ORCA-Flash 4.0 v2; Hamamatsu Photonics) or a CCD camera (ORCA-R2; Hamamatsu Photonics), appropriate filter sets for DAPI/FITC/TRITC, a motorized scanning deck, and an incubation chamber ( $37^\circ\text{C}$ , 5%  $\text{CO}_2$ , 85% humidity; Tokai Hit). All hardware was controlled using MetaMorph (Molecular Devices). The image frame rate was 2 s/frame. To analyze the speed of EBI, we tracked individual EBI comets using the TrackMate plugin version 3.5.1 for Fiji. We selected two sides of the AJC to show EBI comets ([Fig. 6 C](#); [Fig. S5 C](#)). To evaluate the movement of MTs in MCCs, we analyzed the time-lapse images of mEGFP- $\alpha$ -tubulin using the LPX flow plugin (originally called KBI-Flow; [Ueda et al., 2010](#); [https://lpxel.net/products/lpxel-imagej-plugins/](https://lpx.net/products/lpxel-imagej-plugins/)) for ImageJ (National Institutes of Health; freely available at <http://imagej.nih.gov/ij/index.html>).

### Visualization of mucociliary transport

To analyze mucociliary transport, adult mouse tracheal samples were isolated and observed using a fluorescence microscope and a DSU microscope (BX53-DSU; Olympus). The flow of fluorescent beads (a 500-fold dilution of Fluoresbrite, 0.5  $\mu\text{m}$ ; Polysciences) in the mouse trachea was recorded at 25 ms/frame using a water immersion objective lens (LUMPlan FLN 60 $\times$ ; NA 1.00; WD, 2.0 mm; Olympus), an sCMOS camera (ORCA-Flash 4.0 v2; Hamamatsu Photonics), and a thermoplate ( $37^\circ\text{C}$ ; Tokai Hit). Hardware was controlled using MetaMorph software (Molecular Devices). After subtracting images processed by Gaussian Blur from all acquired images in ImageJ, each bead was tracked and analyzed using the TrackMate plugin for Fiji.

### Measurement of BB orientation and alignment

First, the BB and BF positions were manually detected. Then, each BB orientation was determined as the direction from the center of the green ring of the BB toward the center of the magenta dot of the BF ([Fig. 1 D](#)). To validate the variations in BB orientations, we adapted methods for the statistical analysis of directional data ([de Leeuw, 2009](#)). According to the definition described by [Herawati et al. \(2016\)](#), the degree of uniformity of BB orientation is called the  $I_o$ .  $I_o$  is calculated as follows. Each direction of the BF on the BB is represented as a unit vector in two dimensions,  $p_i = (\cos\theta_i, \sin\theta_i)$ , where  $\theta_i$  is the angle between the  $i$ th BB orientation and the horizontal axis. When the detected number of BB-BF pairings is  $N$ , the mean resultant vector  $\bar{r}$  is calculated by:

$$\bar{r} = \frac{1}{N} \sum_{i=1}^N p_i = (|\bar{r}|\cos\bar{\theta}, |\bar{r}|\sin\bar{\theta}).$$

The magnitude of the mean resulting vector  $|\bar{r}|$  is defined as  $I_o$ , where  $I_o$  is bound in the interval  $[0, 1]$ . When  $I_o = 1$ , all BFs point in the same direction; conversely, when  $I_o = 0$ , the direction of BBs is completely random.  $\bar{\theta}$  is the mean angular direction.

$I_o^{\text{cell}}$  and  $I_o^{\text{trachea}}$  are  $I_o$  for a single cell and for multiple cells in the trachea, respectively (see [Fig. 2, A and B](#)). Note that  $I_o^{\text{cell}}$

and  $I_o^{trachea}$  are clearly different in the following points:  $I_o^{trachea}$  indicates the variation in the orientation of BBs around the single mean direction  $\bar{\theta}$  through the trachea under consideration. In contrast,  $I_o^{cell}$  indicates each direction for the cell under consideration. In general, when both the  $I_o^{cell}$  and  $I_o^{trachea}$  scores are high, BF<sub>s</sub> on BBs point in the same direction in the cell and throughout the trachea under consideration. In contrast, when  $I_o^{cell}$  is high and  $I_o^{trachea}$  is low, BF<sub>s</sub> on BBs within each cell point in the same direction, but the mean directions of BF<sub>s</sub> on BBs in respective cells are oriented in different directions.

#### Quantification of apical cytoskeleton intensity in MCCs

Quantification of the apical MT, actin, and keratin 8 labeling intensities was performed using ImageJ. For evaluation of MT intensities, a linear region of interest (ROI) was drawn from the opposite side of the Fzd6 side of the AJC (distance, 0.00) to the Fzd6 side of the AJC (distance, 1.00), and the intensity values of MTs were measured along the linear ROI. To evaluate the increase in MT intensity along the linear ROI, the coefficient of slope of intensity value was analyzed in more than five cells. For the actin or keratin 8 intensities, ROIs were set, and the intensities in them were measured in the regions surrounded by the MCC cell boundaries.

#### MT co-sedimentation assay

Tubulin protein (T240; Cytoskeleton) was polymerized to MTs in PME buffer (80 mM Pipes, 1 mM MgCl<sub>2</sub>, 1 mM EGTA, pH 6.9) containing 1 mM GTP (G8877; Sigma-Aldrich) and 1 mM paclitaxel (M1404; Sigma-Aldrich) at 37°C for 30 min. MTs were diluted to different final concentrations with 20 mM Hepes (pH 7.5), 100 mM KCl, 1 mM DTT (Y00147; Invitrogen), 1 mM GTP, and 10 μM paclitaxel and incubated at 37°C for 15 min with 500 nM purified Daple FL protein. In the MT co-sedimentation assay for Daple domains, MTs were diluted to a final concentration of 10 μM with 20 mM Hepes (pH 7.5), 100 mM KCl, 1 mM DTT, 1 mM GTP, and 10 μM paclitaxel and incubated at 37°C for 15 min with either 750 nM CT domains and 1.2 μM NT domains of Daple or 480 nM Daple ΔCT, respectively. Then, MTs were pelleted by ultracentrifugation at 100,000 × *g* at 37°C for 10 min. Supernatants and pellets were fractionated and applied on SDS-PAGE gels. After electrophoresis, the gels were stained with Coomassie Blue, and the protein band intensities were quantified using ImageJ.

#### IP

HEK293T cells on 10-cm dishes were transiently transfected with 6 μg mEGFP(A206K)-Daple plasmids as appropriate. The cells were washed three times with HBS and then scraped with 300 μl radioimmunoprecipitation assay buffer (50 mM Tris, pH 7.6, 150 mM NaCl, 0.5 wt/vol % sodium deoxycholate, 1.0 wt/vol % NP-40). The cell lysate was clarified using centrifugation at 20,400 × *g* at 4°C for 30 min and incubated with 20 μl protein A-Sepharose bead slurry (17-0780-01; GE Healthcare), which was conjugated in advance with mouse anti-α-tubulin antibodies (T9026; Sigma-Aldrich) or total mouse IgG (0107-01; SouthernBiotech) as a control, at rt for 120 min. After four

washes with radioimmunoprecipitation assay buffer, the IP beads were dissolved in 50 μl SDS sample buffer for SDS-PAGE. The immunoprecipitated proteins were evaluated using immunoblotting.

#### SDS-PAGE and immunoblotting

Equal amounts of proteins were separated using SDS-PAGE on 10–20% gels and transferred to polyvinylidene difluoride membranes. The membranes were then blocked with 5% skim milk or 5% BSA for 30 min, probed with primary antibodies at rt for 60–120 min, and then incubated with HRP-conjugated secondary antibodies at rt for 30–60 min. Immunoblotted bands were visualized with enhanced chemiluminescence (WBKLS0500; Merck Millipore). Densitometric quantification of the SDS-PAGE bands or immunoblotted bands was performed using ImageJ.

#### Preparation of fluorescently labeled MTs

Tubulin was purified from pig brain tissue using a high-molarity Pipes buffer (1 M Pipes-KOH, pH 6.8, 20 mM EGTA, and 10 mM MgCl<sub>2</sub>), as described previously (Castoldi and Popov, 2003). Tubulin was labeled with Cy3 (PA23001; GE Healthcare) or ATTO 647N (AD 647N-31; ATTO-TEC). ATTO 647N-MTs were polymerized by co-polymerizing with labeled and unlabeled tubulin at a ratio of 1:5 at 37°C for 30 min in the presence of taxol (T1912; Sigma-Aldrich).

#### Quantification of fluorescence signal intensities of purified proteins on glass surfaces

Quantification of fluorescence signal intensities was performed as previously described (Yukawa et al., 2019). Flow chambers were assembled from two coverslips (18 × 18 mm and 24 × 32 mm; Matsunami Glass) with two slivers of parafilm as a spacer. The coverslips were heat sealed on a 98°C hot plate. mEGFP-tagged proteins were appropriately diluted in BRB12 buffer (12 mM Pipes, pH 6.8, adjusted with NaOH, 2 mM MgCl<sub>2</sub>, and 1 mM EGTA) supplemented with 2 mM DTT, 25 mM glucose, 21.3 U/ml glucose oxidase (G2133; Sigma-Aldrich), and 800 U/ml catalase (219001; Merck Millipore) and then perfused into the flow chamber.

Fluorescence spots were imaged using an objective-type Nikon TIRFM system (Eclipse Ti-E; Nikon Corp.) equipped with a 488-nm laser (488-75CDRH; Coherent) and a 60×/NA 1.49 oil immersion objective lens (CFI Apo TIRF 60×H; Nikon) at 24 ± 1°C. Images were magnified using a 2.5× TV-adaptor (MQD42120; Nikon) and projected onto an EM CCD detector (C9100-13; Hamamatsu Photonics). The camera was controlled using Micro-Manager software version 1.4.2243. The photo-bleaching behavior of mEGFP-Daple was analyzed by summing the intensities from a 10 × 10-pixel region and subtracting the mean intensity of the three regions around each fluorescence spot as background intensity after four-frame rolling averaging using the Running Z projector plugin for ImageJ. To obtain the intensity profile of mEGFP-labeled proteins adsorbed onto a glass surface, the TrackMate plugin for Fiji was used to automatically detect and quantify the intensities of fluorescence spots. A difference of Gaussian detector with an estimated diameter of 10 pixels was used.

### Single-molecule assay for Daple

To immobilize MTs, a dimethyldichlorosilane-treated flow chamber was incubated with 1:10 diluted anti-tubulin antibody (66031-1-Ig; Proteintech) in BRB80 buffer (80 mM Pipes, 1 mM EGTA, 1 mM MgCl<sub>2</sub>, pH 6.9) for 5 min and blocked with 1% wt/vol Pluronic F-127 in BRB80 buffer. After washing with BRB80 buffer, ATTO 647N-labeled MTs in BRB80 buffer were perfused and incubated for 5 min. After further washing with 0.6–0.7 mg/ml casein in BRB12 buffer (12 mM Pipes, 1 mM EGTA, 1 mM MgCl<sub>2</sub>, pH 6.9), the final solution containing mEGFP-Daple protein in BRB12 buffer (containing 10 μM paclitaxel, 2 mM DTT, 25 mM glucose, 21.3 U/ml glucose oxidase, 800 U/ml catalase, and 0.7 mg/ml casein) was added to the flow chamber.

The single-molecule behavior of mEGFP-Daple was imaged using the same setup as described above for the intensity measurement, except that a 632.8-nm laser (30991; Research Electro Optics) was used with a 488-nm laser (488-75CDRH; Coherent) for TIRF illumination. The video frame rate was 100 ms/frame. The signal intensity of mEGFP-Daple along MTs was measured using ImageJ.

To examine the MT bundling ability of mEGFP-Daple, ATTO 647N-labeled MTs were mixed with 10 nM mEGFP-Daple or its domains and incubated at rt for 10 min. The mixture was then added to the flow chamber. Samples were imaged using a 632.8-nm laser (30991; Research Electro Optics) and a 488-nm laser (488-75CDRH; Coherent) for TIRF illumination.

### TEM and UHVEMT

After isolating either the trachea or cultured cells, the samples were fixed with 0.1% tannic acid, 2% formaldehyde, and 2.5% glutaraldehyde in 100 mM Hepes buffer (pH 7.5) at 37°C for 1 h, followed by postfixation with 1% OsO<sub>4</sub> in 100 mM Hepes buffer (pH 7.5) on ice for 2 h, as previously described (Tsukita et al., 1980). The samples were dehydrated and embedded in Poly/Bed 812 (08791-500; Polysciences). For TEM, the samples were serially sectioned at either 50 nm or 70 nm and analyzed using a JEM-1400 plus microscope (JEOL). For UHVEMT, the samples were sectioned at 700 nm and mounted on formvar-coated 50-mesh copper grids (Nisshin-EM). Colloidal gold particles (20-nm diameter) were deposited on each section, and the samples were observed at an acceleration voltage of 1 MeV (H-3000; Hitachi). Images were taken at 25,000× magnification from –60° to +66° at 2° intervals around a single-tilt axis and acquired with a slow scan CCD camera (model F415S; TVIPS GmbH). The image calibration and 3D reconstructions of each series were performed using IMOD software (Kremer et al., 1996).

### Negative stain EM

MTs were incubated with 10 nM Daple in 20 mM Hepes (pH 7.5), 150 mM NaCl, 10 μM paclitaxel, 1 mM DTT, and 1 mM GTP at rt for 10 min. The mixture was loaded onto carbon-coated, glow-discharged 400-mesh copper grids and incubated for 10 min. The grid was stained in a drop of 4% uranyl acetate and air dried. Samples were analyzed using JEM-1400 plus (JEOL).

### Statistical analyses

The data in boxplots are presented as medians, 25th–75th percentiles, ranges, and outliers. Error bars were defined as the 95%

confidence interval. Statistical analysis was performed on at least three biological replicates under similar conditions using the statistical software R version 3.6.3 (freely available at <https://www.r-project.org>). The normality of the data distribution was tested using the Shapiro-Wilk test, and either a parametric or nonparametric statistical method was selected. A nonparametric statistical method was used for small-sample-size data ( $n < 9$ ). For nonparametric analyses, Mann-Whitney *U* tests and Kruskal-Wallis tests with Steel-Dwass multiple-comparison tests and Fisher's exact tests with Benjamini-Hochberg multiple-comparison tests were used. For parametric analyses, one-way ANOVA with Tukey-Kramer multiple-comparison tests were used. Data are presented as mean ± SE. Results with  $P < 0.05$  were considered statistically significant.

### Online supplemental material

**Fig. S1** depicts the localization of Daple in WT trachea and mucociliary transport in WT, Daple-KO, and Vangl1-KO tracheas. **Fig. S2** displays the localization of the core PCP proteins in WT, Daple-KO, and Vangl1-KO tracheas. **Fig. S3** presents analyses of cytoskeletons in WT and Daple-KO MCCs in MTECs. **Fig. S4** shows that the nocodazole treatment did not affect the localization of core PCP proteins, such as Fzd6, and that GBA mutation did not affect the polarized localization of apical MTs. **Fig. S5** details the localization of EB1 in WT MTECs and the EB1 dynamics in Daple-KO MCCs. **Video 1** shows live imaging of fluorescent beads in WT, Daple-KO, and Vangl1-KO adult tracheas. **Video 2** shows superresolution imaging of MTs at different z-slices in WT MCCs of MTECs. **Video 3** shows the image of apical MTs revealed by UHVEMT in WT and Daple-KO adult tracheas. **Videos 4** and **5** show live imaging of EB1 in WT (**Video 4**) and Daple-KO (**Video 5**) MCCs of MTECs. **Video 6** shows live imaging of α-tubulin in WT and Daple-KO MCCs of MTECs. **Video 7** shows live imaging of a single Daple molecule along an MT. **Video 8** shows the UHVEMT image of MTs and bundling of MTs in WT MCCs.

### Acknowledgments

We are grateful to our laboratory members for helpful discussions, particularly Dr. Hiroo Tanaka, Dr. Timothy Day, Dr. Hiroka Kashihara, and Kazuto Tsukita. We especially thank Fumiko Takenaga, Mariko Hata, and Miho Sawada for their technical assistance. We are grateful to Dr. Toshihisa Ohtsuka (Yamanashi University, Yamanashi, Japan) for the gift of rabbit anti-prickle2 pAb. We thank Dr. Toshihiko Fujimori (National Institute for Basic Biology, Aichi, Japan) for providing us with the Vangl1<sup>gt</sup> mice. We are grateful to Dr. Michael Z. Lin for providing us with the pNCS-mRuby3 vector. We thank Dr. Yasushi Okamura and Dr. Makoto Adachi for their discussions and suggestions. We are thankful to Editage (<https://www.editage.com>) for English language editing.

This work was supported by the Core Research for Evolutionary Science and Technology program of the Japan Science and Technology Agency (to S. Tsukita); by the Japan Society for the Promotion of Science through a Grant-in-Aid for Specially Promoted Research (grant JP19H05468 to S. Tsukita), a Grant-

in-Aid for Early-Career Scientists (grant JP18K14696 to T. Yano), and a Grant-in-Aid for Scientific Research (grant JP16H05121 to A. Tamura); by a research grant from the Takeda Science Foundation (to S. Tsukita); by the Uehara Memorial Foundation (to S. Tsukita); and by the Kobayashi Foundation (to S. Tsukita).

The authors declare no competing financial interests.

Author contributions: Conception of the work: S. Nakayama, T. Yano, and S. Tsukita. Experimental design: S. Nakayama, T. Yano, T. Namba, K. Furuta, K. Oiwa, and S. Tsukita. Acquisition of data: S. Nakayama, T. Yano, S. Konishi, T. Nishida, K. Furuta, and K. Oiwa. Data analysis: S. Nakayama, T. Yano, T. Namba, T. Nishida, S. Konishi, K. Furuta, K. Oiwa, and S. Tsukita. Data interpretation: S. Nakayama, T. Yano, T. Namba, M. Takagishi, E. Herawati, Y. Imoto, A. Tamura, S. Ishihara, M. Takahashi, K. Furuta, K. Oiwa, and S. Tsukita. Drafting of the manuscript: S. Nakayama, T. Yano, T. Namba, K. Furuta, and S. Tsukita.

Submitted: 9 October 2020

Revised: 9 March 2021

Accepted: 22 March 2021

## References

- Antoniades, I., P. Stylianou, and P.A. Skourides. 2014. Making the connection: ciliary adhesion complexes anchor basal bodies to the actin cytoskeleton. *Dev. Cell.* 28:70–80. <https://doi.org/10.1016/j.devcel.2013.12.003>
- Aw, W.Y., and D. Devenport. 2017. Planar cell polarity: global inputs establishing cellular asymmetry. *Curr. Opin. Cell Biol.* 44:110–116. <https://doi.org/10.1016/j.cob.2016.08.002>
- Aznar, N., K.K. Midde, Y. Dunkel, I. Lopez-Sanchez, Y. Pavlova, A. Marivin, J. Barbazán, F. Murray, U. Nitsche, K.P. Janssen, et al. 2015. Daple is a novel non-receptor GEF required for trimeric G protein activation in Wnt signaling. *eLife.* 4:e07091. <https://doi.org/10.7554/eLife.07091>
- Aznar, N., J. Ear, Y. Dunkel, N. Sun, K. Satterfield, F. He, N.A. Kalogriopoulos, I. Lopez-Sanchez, M. Ghassemian, D. Sahoo, et al. 2018. Convergence of Wnt, growth factor, and heterotrimeric G protein signals on the guanine nucleotide exchange factor Daple. *Sci. Signal.* 11:ea04220. <https://doi.org/10.1126/scisignal.aao4220>
- Bajar, B.T., E.S. Wang, A.J. Lam, B.B. Kim, C.L. Jacobs, E.S. Howe, M.W. Davidson, M.Z. Lin, and J. Chu. 2016. Improving brightness and photostability of green and red fluorescent proteins for live cell imaging and FRET reporting. *Sci. Rep.* 6:20889. <https://doi.org/10.1038/srep20889>
- Bayless, B.A., D.F. Galati, A.D. Junker, C.B. Backer, J. Gaertig, and C.G. Pearson. 2016. Asymmetrically localized proteins stabilize basal bodies against ciliary beating forces. *J. Cell Biol.* 215:457–466. <https://doi.org/10.1083/jcb.201604135>
- Bodakuntla, S., A.S. Jijumon, C. Villablanca, C. Gonzalez-Billault, and C. Janke. 2019. Microtubule-associated proteins: structuring the cytoskeleton. *Trends Cell Biol.* 29:804–819. <https://doi.org/10.1016/j.tcb.2019.07.004>
- Boutin, C., P. Labeledan, J. Dimidschstein, F. Richard, H. Cremer, P. André, Y. Yang, M. Montcouquiol, A.M. Goffinet, and F. Tisser. 2014. A dual role for planar cell polarity genes in ciliated cells. *Proc. Natl. Acad. Sci. USA.* 111:E3129–E3138. <https://doi.org/10.1073/pnas.1404988111>
- Boutros, M., N. Paricio, D.I. Strutt, and M. Mlodzik. 1998. Dishevelled activates JNK and discriminates between JNK pathways in planar polarity and wingless signaling. *Cell.* 94:109–118. [https://doi.org/10.1016/S0092-8674\(00\)81226-X](https://doi.org/10.1016/S0092-8674(00)81226-X)
- Brooks, E.R., and J.B. Wallingford. 2014. Multiciliated cells. *Curr. Biol.* 24:R973–R982. <https://doi.org/10.1016/j.cub.2014.08.047>
- Burkart, G.M., and R. Dixit. 2019. Microtubule bundling by MAP65-1 protects against severing by inhibiting the binding of katanin. *Mol. Biol. Cell.* 30:1587–1597. <https://doi.org/10.1091/mbc.E18-12-0776>
- Bustamante-Marin, X.M., and L.E. Ostrowski. 2017. Cilia and mucociliary clearance. *Cold Spring Harb. Perspect. Biol.* 9:a028241. <https://doi.org/10.1101/cshperspect.a028241>
- Butler, M.T., and J.B. Wallingford. 2017. Planar cell polarity in development and disease. *Nat. Rev. Mol. Cell Biol.* 18:375–388. <https://doi.org/10.1038/nrm.2017.11>
- Carvajal-Gonzalez, J.M., S. Mulero-Navarro, and M. Mlodzik. 2016a. Centriole positioning in epithelial cells and its intimate relationship with planar cell polarity. *BioEssays.* 38:1234–1245. <https://doi.org/10.1002/bies.201600154>
- Carvajal-Gonzalez, J.M., A.-C. Roman, and M. Mlodzik. 2016b. Positioning of centrioles is a conserved readout of Frizzled planar cell polarity signaling. *Nat. Commun.* 7:11135. <https://doi.org/10.1038/ncomms11135>
- Castoldi, M., and A.V. Popov. 2003. Purification of brain tubulin through two cycles of polymerization-depolymerization in a high-molarity buffer. *Protein Expr. Purif.* 32:83–88. [https://doi.org/10.1016/S1046-5928\(03\)00218-3](https://doi.org/10.1016/S1046-5928(03)00218-3)
- Chien, Y.-H., R. Keller, C. Kintner, and D.R. Shook. 2015. Mechanical strain determines the axis of planar polarity in ciliated epithelia. *Curr. Biol.* 25:2774–2784. <https://doi.org/10.1016/j.cub.2015.09.015>
- Ciani, L., O. Krylova, M.J. Smalley, T.C. Dale, and P.C. Salinas. 2004. A divergent canonical WNT-signaling pathway regulates microtubule dynamics: dishevelled signals locally to stabilize microtubules. *J. Cell Biol.* 164:243–253. <https://doi.org/10.1083/jcb.200309096>
- Dasgupta, A., and J.D. Amack. 2016. Cilia in vertebrate left-right patterning. *Philos. Trans. R. Soc. Lond. B Biol. Sci.* 371:20150410. <https://doi.org/10.1098/rstb.2015.0410>
- Davey, C.F., and C.B. Moens. 2017. Planar cell polarity in moving cells: think globally, act locally. *Development.* 144:187–200. <https://doi.org/10.1242/dev.122804>
- de Leeuw, J. 2009. Journal of Statistical Software. *WIREs Comp. Stat.* 1:128–129. <https://doi.org/10.1002/wics.10>
- Devenport, D. 2014. The cell biology of planar cell polarity. *J. Cell Biol.* 207:171–179. <https://doi.org/10.1083/jcb.201408039>
- Ear, J., A. Saklecha, N. Rajapakse, J. Choi, M. Ghassemian, I. Kufareva, and P. Ghosh. 2020. Tyrosine-based signals regulate the assembly of Daple-PARD3 complex at cell-cell junctions. *iScience.* 23:100859. <https://doi.org/10.1016/j.isci.2020.100859>
- Eaton, S. 1997. Planar polarization of *Drosophila* and vertebrate epithelia. *Curr. Opin. Cell Biol.* 9:860–866. [https://doi.org/10.1016/S0955-0674\(97\)80089-0](https://doi.org/10.1016/S0955-0674(97)80089-0)
- Fuertes-Alvarez, S., L. Maeso-Alonso, J. Villoch-Fernandez, M. Wildung, M. Martin-Lopez, C. Marshall, A.J. Villena-Cortes, I. Diez-Prieto, J.A. Pientepol, F. Tissir, et al. 2018. p73 regulates ependymal planar cell polarity by modulating actin and microtubule cytoskeleton. *Cell Death Dis.* 9:1183. <https://doi.org/10.1038/s41419-018-1205-6>
- Garcia, G. III, and J.F. Reiter. 2016. A primer on the mouse basal body. *Cilia.* 5:17. <https://doi.org/10.1186/s13630-016-0038-0>
- Goodrich, L.V., and D. Strutt. 2011. Principles of planar polarity in animal development. *Development.* 138:1877–1892. <https://doi.org/10.1242/dev.054080>
- Graham, F.L., J. Smiley, W.C. Russell, and R. Nairn. 1977. Characteristics of a human cell line transformed by DNA from human adenovirus type 5. *J. Gen. Virol.* 36:59–74. <https://doi.org/10.1099/0022-1317-36-1-59>
- Gromley, A., A. Jurczyk, J. Sillibourne, E. Halilovic, M. Mogensen, I. Groisman, M. Blomberg, and S. Doherty. 2003. A novel human protein of the maternal centriole is required for the final stages of cytokinesis and entry into S phase. *J. Cell Biol.* 161:535–545. <https://doi.org/10.1083/jcb.200301105>
- Guirao, B., A. Meunier, S. Mortaud, A. Aguilar, J.M. Corsi, L. Strehl, Y. Hirota, A. Desoeuvre, C. Boutin, Y.G. Han, et al. 2010. Coupling between hydrodynamic forces and planar cell polarity orients mammalian motile cilia. *Nat. Cell Biol.* 12:341–350. <https://doi.org/10.1038/ncb2040>
- Haag, N., S. Schüler, S. Nietzsche, C.A. Hübner, N. Strenzke, B. Qualmann, and M.M. Kessels. 2018. The actin nucleator Cobl is critical for centriolar positioning, postnatal planar cell polarity refinement, and function of the cochlea. *Cell Rep.* 24:2418–2431.e6. <https://doi.org/10.1016/j.celrep.2018.07.087>
- Habas, R., Y. Kato, and X. He. 2001. Wnt/Frizzled activation of Rho regulates vertebrate gastrulation and requires a novel Formin homology protein Daam1. *Cell.* 107:843–854. [https://doi.org/10.1016/S0092-8674\(01\)00614-6](https://doi.org/10.1016/S0092-8674(01)00614-6)
- Herawati, E., D. Taniguchi, H. Kanoh, K. Tateishi, S. Ishihara, and S. Tsukita. 2016. Multiciliated cell basal bodies align in stereotypical patterns coordinated by the apical cytoskeleton. *J. Cell Biol.* 214:571–586. <https://doi.org/10.1083/jcb.201601023>
- Higginbotham, H., S. Bielas, T. Tanaka, and J.G. Gleeson. 2004. Transgenic mouse line with green-fluorescent protein-labeled Centrin 2 allows visualization of the centrosome in living cells. *Transgenic Res.* 13:155–164. <https://doi.org/10.1023/B:TRAG.0000026071.41735.8e>
- Horani, A., T.W. Ferkol, S.K. Dutcher, and S.L. Brody. 2016. Genetics and biology of primary ciliary dyskinesia. *Paediatr. Respir. Rev.* 18:18–24. <https://doi.org/10.1016/j.prrv.2015.09.001>

- Hudspeth, A.J. 2014. Integrating the active process of hair cells with cochlear function. *Nat. Rev. Neurosci.* 15:600–614. <https://doi.org/10.1038/nrn3786>
- Ishida-Takagishi, M., A. Enomoto, N. Asai, K. Ushida, T. Watanabe, T. Hashimoto, T. Kato, L. Weng, S. Matsumoto, M. Asai, et al. 2012. The Dishevelled-associating protein Daple controls the non-canonical Wnt/Rac pathway and cell motility. *Nat. Commun.* 3:859. <https://doi.org/10.1038/ncomms1861>
- Ishikawa, H., A. Kubo, S. Tsukita, and S. Tsukita. 2005. Odf2-deficient mother centrioles lack distal/subdistal appendages and the ability to generate primary cilia. *Nat. Cell Biol.* 7:517–524. <https://doi.org/10.1038/ncb1251>
- Kashihara, H., S. Chiba, S.I. Kanno, K. Suzuki, T. Yano, and S. Tsukita. 2019. Cep128 associates with Odf2 to form the subdistal appendage of the centriole. *Genes Cells.* 24:231–243. <https://doi.org/10.1111/gtc.12668>
- Kikuchi, K., A. Nakamura, M. Arata, D. Shi, M. Nakagawa, T. Tanaka, T. Uemura, T. Fujimori, A. Kikuchi, A. Uezu, et al. 2018. Map7/7D1 and Dvl form a feedback loop that facilitates microtubule remodeling and Wnt5a signaling. *EMBO Rep.* 19:1–20. <https://doi.org/10.15252/embr.201745471>
- Kim, S.K., S. Zhang, M.E. Werner, E.J. Brotslaw, J.W. Mitchell, M.M. Altabbaa, and B.J. Mitchell. 2018. CLAMP/Spchl1 regulates planar cell polarity signaling and asymmetric microtubule accumulation in the *Xenopus* ciliated epithelia. *J. Cell Biol.* 217:1633–1641. <https://doi.org/10.1083/jcb.201706058>
- Kremer, J.R., D.N. Mastrorade, and J.R. McIntosh. 1996. Computer visualization of three-dimensional image data using IMOD. *J. Struct. Biol.* 116:71–76. <https://doi.org/10.1006/jmbi.1996.0013>
- Krylova, O., M.J. Messinger, and P.C. Salinas. 2000. Dishevelled-1 regulates microtubule stability: a new function mediated by glycogen synthase kinase-3 $\beta$ . *J. Cell Biol.* 151:83–94. <https://doi.org/10.1083/jcb.151.1.83>
- Kunimoto, K., Y. Yamazaki, T. Nishida, K. Shinohara, H. Ishikawa, T. Hasegawa, T. Okanoue, H. Hamada, T. Noda, A. Tamura, et al. 2012. Coordinated ciliary beating requires Odf2-mediated polarization of basal bodies via basal feet. *Cell.* 148:189–200. <https://doi.org/10.1016/j.cell.2011.10.052>
- Landin Malt, A., Z. Dailey, J. Holbrook-Rasmussen, Y. Zheng, A. Hogan, Q. Du, and X. Lu. 2019. Par3 is essential for the establishment of planar cell polarity of inner ear hair cells. *Proc. Natl. Acad. Sci. USA.* 116:4999–5008. <https://doi.org/10.1073/pnas.1816333116>
- Landin Malt, A., A.K. Hogan, C.D. Smith, M.S. Madani, and X. Lu. 2020. Wnts regulate planar cell polarity via heterotrimeric G protein and PI3K signaling. *J. Cell Biol.* 219:e201912071. <https://doi.org/10.1083/jcb.201912071>
- Lee, M., Y.-S. Hwang, J. Yoon, J. Sun, A. Harned, K. Nagashima, and I.O. Daar. 2019. Developmentally regulated GTP-binding protein 1 modulates ciliogenesis via an interaction with Dishevelled. *J. Cell Biol.* 218:2659–2676. <https://doi.org/10.1083/jcb.201811147>
- Leyme, A., A. Marivin, M. Maziarz, V. DiGiacomo, M.P. Papakonstantinou, P.P. Patel, J.B. Blanco-Canosa, I.A. Walawalkar, G. Rodriguez-Davila, I. Dominguez, and M. Garcia-Marcos. 2017. Specific inhibition of GPCR-independent G protein signaling by a rationally engineered protein. *Proc. Natl. Acad. Sci. USA.* 114:E10319–E10328. <https://doi.org/10.1073/pnas.1707992114>
- Marivin, A., and M. Garcia-Marcos. 2019. DAPLE and MPDZ bind to each other and cooperate to promote apical cell constriction. *Mol. Biol. Cell.* 30:1900–1910. <https://doi.org/10.1091/mbc.E19-02-0091>
- Marivin, A., V. Morozova, I. Walawalkar, A. Leyme, D.A. Kretov, D. Cifuentes, I. Dominguez, and M. Garcia-Marcos. 2019. GPCR-independent activation of G proteins promotes apical cell constriction in vivo. *J. Cell Biol.* 218:1743–1763. <https://doi.org/10.1083/jcb.201811174>
- Marivin, A., M. Maziarz, J. Zhao, V. DiGiacomo, I. Olmos Calvo, E.A. Mann, J. Ear, J.B. Blanco-Canosa, E.M. Ross, P. Ghosh, and M. Garcia-Marcos. 2020. DAPLE protein inhibits nucleotide exchange on G $\alpha_q$  and G $\alpha_q$  via the same motif that activates G $\alpha_i$ . *J. Biol. Chem.* 295:2270–2284. <https://doi.org/10.1074/jbc.RA119.011648>
- Mlodzik, M. 2020. Planar cell polarity: moving from single cells to tissue-scale biology. *Development.* 147:dev186346. <https://doi.org/10.1242/dev.186346>
- Nakagawa, Y., Y. Yamane, T. Okanoue, S. Tsukita, and S. Tsukita. 2001. Outer dense fiber 2 is a widespread centrosome scaffold component preferentially associated with mother centrioles: its identification from isolated centrosomes. *Mol. Biol. Cell.* 12:1687–1697. <https://doi.org/10.1091/mbc.12.6.1687>
- Namba, T., and S. Ishihara. 2020. Cytoskeleton polarity is essential in determining orientational order in basal bodies of multi-ciliated cells. *PLOS Comput. Biol.* 16:e1007649. <https://doi.org/10.1371/journal.pcbi.1007649>
- Ohata, S., J. Nakatani, V. Herranz-Pérez, J. Cheng, H. Belinson, T. Inubushi, W.D. Snider, J.M. García-Verdugo, A. Wynshaw-Boris, and A. Álvarez-Buylla. 2014. Loss of Dishevelleds disrupts planar polarity in ependymal motile cilia and results in hydrocephalus. *Neuron.* 83:558–571. <https://doi.org/10.1016/j.neuron.2014.06.022>
- Oshita, A., S. Kishida, H. Kobayashi, T. Michiue, T. Asahara, M. Asashima, and A. Kikuchi. 2003. Identification and characterization of a novel Dvl-binding protein that suppresses Wnt signalling pathway. *Genes Cells.* 8:1005–1017. <https://doi.org/10.1111/j.1365-2443.2003.00692.x>
- Park, T.J., B.J. Mitchell, P.B. Abitua, C. Kintner, and J.B. Wallingford. 2008. Dishevelled controls apical docking and planar polarization of basal bodies in ciliated epithelial cells. *Nat. Genet.* 40:871–879. <https://doi.org/10.1038/ng.104>
- Reiter, J.F., and M.R. Leroux. 2017. Genes and molecular pathways underpinning ciliopathies. *Nat. Rev. Mol. Cell Biol.* 18:533–547. <https://doi.org/10.1038/nrm.2017.60>
- Roberson, E.C., N.K. Tran, M.J. Konjikusic, R.D. Fitch, R.S. Gray, and J.B. Wallingford. 2020. A comparative study of the turnover of multiciliated cells in the mouse trachea, oviduct, and brain. *Dev. Dyn.* 249:898–905. <https://doi.org/10.1002/dvdy.165>
- Shi, D., F. Usami, K. Komatsu, S. Oka, T. Abe, T. Uemura, and T. Fujimori. 2016. Dynamics of planar cell polarity protein Vangl2 in the mouse oviduct epithelium. *Mech. Dev.* 141:78–89. <https://doi.org/10.1016/j.mdev.2016.05.002>
- Shimada, Y., S. Yonemura, H. Ohkura, D. Strutt, and T. Uemura. 2006. Polarized transport of Frizzled along the planar microtubule arrays in *Drosophila* wing epithelium. *Dev. Cell.* 10:209–222. <https://doi.org/10.1016/j.devcel.2005.11.016>
- Siletti, K., B. Tarchini, and A.J. Hudspeth. 2017. Daple coordinates organ-wide and cell-intrinsic polarity to pattern inner-ear hair bundles. *Proc. Natl. Acad. Sci. USA.* 114:E11170–E11179. <https://doi.org/10.1073/pnas.1716522115>
- Singh, A., T. Saha, I. Begemann, A. Ricker, H. Nüsse, O. Thorn-Seshold, J. Klingauf, M. Galic, and M. Matis. 2018. Polarized microtubule dynamics directs cell mechanics and coordinates forces during epithelial morphogenesis. *Nat. Cell Biol.* 20:1126–1133. <https://doi.org/10.1038/s41556-018-0193-1>
- Sipe, C.W., L. Liu, J. Lee, C. Grimsley-Myers, and X. Lu. 2013. Lis1 mediates planar polarity of auditory hair cells through regulation of microtubule organization. *Development.* 140:1785–1795. <https://doi.org/10.1242/dev.089763>
- Skarnes, W.C., B. Rosen, A.P. West, M. Koutsourakis, W. Bushell, V. Iyer, A.O. Mujica, M. Thomas, J. Harrow, T. Cox, et al. 2011. A conditional knockout resource for the genome-wide study of mouse gene function. *Nature.* 474:337–342. <https://doi.org/10.1038/nature10163>
- Soh, A.W.J., T.J.P. van Dam, A.J. Stemm-Wolf, A.T. Pham, G.P. Morgan, E.T. O'Toole, and C.G. Pearson. 2020. Ciliary force-responsive striated fibers promote basal body connections and cortical interactions. *J. Cell Biol.* 219:e201904091. <https://doi.org/10.1083/jcb.201904091>
- Song, H., J. Hu, W. Chen, G. Elliott, P. Andre, B. Gao, and Y. Yang. 2010. Planar cell polarity breaks bilateral symmetry by controlling ciliary positioning. *Nature.* 466:378–382. <https://doi.org/10.1038/nature09129>
- Spassky, N., and A. Meunier. 2017. The development and functions of multiciliated epithelia. *Nat. Rev. Mol. Cell Biol.* 18:423–436. <https://doi.org/10.1038/nrm.2017.21>
- Steyger, P.S., D.N. Furness, C.M. Hackney, and G.P. Richardson. 1989. Tubulin and microtubules in cochlear hair cells: comparative immunocytochemistry and ultrastructure. *Hear. Res.* 42:1–16. [https://doi.org/10.1016/0378-5955\(89\)90113-5](https://doi.org/10.1016/0378-5955(89)90113-5)
- Strutt, D.I., U. Weber, and M. Mlodzik. 1997. The role of RhoA in tissue polarity and Frizzled signalling. *Nature.* 387:292–295. <https://doi.org/10.1038/387292a0>
- Subramanian, R., E.M. Wilson-Kubalek, C.P. Arthur, M.J. Bick, E.A. Campbell, S.A. Darst, R.A. Milligan, and T.M. Kapoor. 2010. Insights into anti-parallel microtubule crosslinking by PRC1, a conserved nonmotor microtubule binding protein. *Cell.* 142:433–443. <https://doi.org/10.1016/j.cell.2010.07.012>
- Takagishi, M., M. Sawada, S. Ohata, N. Asai, A. Enomoto, K. Takahashi, L. Weng, K. Ushida, H. Ara, S. Matsui, et al. 2017. Daple coordinates planar polarized microtubule dynamics in ependymal cells and contributes to hydrocephalus. *Cell Rep.* 20:960–972. <https://doi.org/10.1016/j.celrep.2017.06.089>
- Takagishi, M., N. Esaki, K. Takahashi, and M. Takahashi. 2020. Cytoplasmic dynein functions in planar polarization of basal bodies within ciliated cells. *iScience.* 23:101213. <https://doi.org/10.1016/j.isci.2020.101213>

- Tateishi, K., Y. Yamazaki, T. Nishida, S. Watanabe, K. Kunimoto, H. Ishikawa, and S. Tsukita. 2013. Two appendages homologous between basal bodies and centrioles are formed using distinct Odf2 domains. *J. Cell Biol.* 203:417–425. <https://doi.org/10.1083/jcb.201303071>
- Tateishi, K., T. Nishida, K. Inoue, and S. Tsukita. 2017. Three-dimensional organization of layered apical cytoskeletal networks associated with mouse airway tissue development. *Sci. Rep.* 7:43783. <https://doi.org/10.1038/srep43783>
- Tilley, A.E., M.S. Walters, R. Shaykhiyev, and R.G. Crystal. 2015. Cilia dysfunction in lung disease. *Annu. Rev. Physiol.* 77:379–406. <https://doi.org/10.1146/annurev-physiol-021014-071931>
- Tissir, F., Y. Qu, M. Montcouquiol, L. Zhou, K. Komatsu, D. Shi, T. Fujimori, J. Labeau, D. Tyteca, P. Courtoy, et al. 2010. Lack of cadherins Celsr2 and Celsr3 impairs ependymal ciliogenesis, leading to fatal hydrocephalus. *Nat. Neurosci.* 13:700–707. <https://doi.org/10.1038/nn.2555>
- Toya, M., and M. Takeichi. 2016. Organization of non-centrosomal microtubules in epithelial cells. *Cell Struct. Funct.* 41:127–135. <https://doi.org/10.1247/csf.16015>
- Tsukita, S., S. Tsukita, and H. Ishikawa. 1980. Cytoskeletal network underlying the human erythrocyte membrane. Thin-section electron microscopy. *J. Cell Biol.* 85:567–576. <https://doi.org/10.1083/jcb.85.3.567>
- Tsukita, K., T. Yano, A. Tamura, and S. Tsukita. 2019a. Reciprocal association between the apical junctional complex and AMPK: a promising therapeutic target for epithelial/endothelial barrier function? *Int. J. Mol. Sci.* 20:6012. <https://doi.org/10.3390/ijms20236012>
- Tsukita, S., H. Tanaka, and A. Tamura. 2019b. The claudins: from tight junctions to biological systems. *Trends Biochem. Sci.* 44:141–152. <https://doi.org/10.1016/j.tibs.2018.09.008>
- Tsukita, S., T. Yano, and E. Herawati. 2020. Apical cytoskeletons help define the barrier functions of epithelial cell sheets in biological systems. *In Make Life Visible.* Y. Toyama, A. Miyawaki, M. Nakamura, and M. Jinzaki, editors. Springer Nature Singapore, Singapore. 31–38. [https://doi.org/10.1007/978-981-13-7908-6\\_4](https://doi.org/10.1007/978-981-13-7908-6_4)
- Ueda, H., E. Yokota, N. Kutsuna, T. Shimada, K. Tamura, T. Shimmen, S. Hasezawa, V.V. Dolja, and I. Hara-Nishimura. 2010. Myosin-dependent endoplasmic reticulum motility and F-actin organization in plant cells. *Proc. Natl. Acad. Sci. USA.* 107:6894–6899. <https://doi.org/10.1073/pnas.0911482107>
- Vladar, E.K., D. Antic, and J.D. Axelrod. 2009. Planar cell polarity signaling: the developing cell's compass. *Cold Spring Harb. Perspect. Biol.* 1:a002964. <https://doi.org/10.1101/cshperspect.a002964>
- Vladar, E.K., R.D. Bayly, A.M. Sangoram, M.P. Scott, and J.D. Axelrod. 2012. Microtubules enable the planar cell polarity of airway cilia. *Curr. Biol.* 22:2203–2212. <https://doi.org/10.1016/j.cub.2012.09.046>
- Wallingford, J.B. 2010. Planar cell polarity signaling, cilia and polarized ciliary beating. *Curr. Opin. Cell Biol.* 22:597–604. <https://doi.org/10.1016/j.cob.2010.07.011>
- Werner, M.E., P. Hwang, F. Huisman, P. Taborek, C.C. Yu, and B.J. Mitchell. 2011. Actin and microtubules drive differential aspects of planar cell polarity in multiciliated cells. *J. Cell Biol.* 195:19–26. <https://doi.org/10.1083/jcb.201106110>
- Winter, C.G., B. Wang, A. Ballew, A. Royou, R. Karess, J.D. Axelrod, and L. Luo. 2001. Drosophila Rho-associated kinase (Drok) links Frizzled-mediated planar cell polarity signaling to the actin cytoskeleton. *Cell.* 105:81–91. [https://doi.org/10.1016/S0092-8674\(01\)00298-7](https://doi.org/10.1016/S0092-8674(01)00298-7)
- Yang, Y., and M. Mlodzik. 2015. Wnt-Frizzled/planar cell polarity signaling: cellular orientation by facing the wind (Wnt). *Annu. Rev. Cell Dev. Biol.* 31:623–646. <https://doi.org/10.1146/annurev-cellbio-100814-125315>
- Yano, T., T. Matsui, A. Tamura, M. Uji, and S. Tsukita. 2013. The association of microtubules with tight junctions is promoted by cingulin phosphorylation by AMPK. *J. Cell Biol.* 203:605–614. <https://doi.org/10.1083/jcb.201304194>
- Yano, T., H. Kanoh, A. Tamura, and S. Tsukita. 2017. Apical cytoskeletons and junctional complexes as a combined system in epithelial cell sheets. *Ann. N. Y. Acad. Sci.* 1405:32–43. <https://doi.org/10.1111/nyas.13432>
- Yano, T., T. Torisawa, K. Oiwa, and S. Tsukita. 2018. AMPK-dependent phosphorylation of cingulin reversibly regulates its binding to actin filaments and microtubules. *Sci. Rep.* 8:15550. <https://doi.org/10.1038/s41598-018-33418-7>
- Yano, T., K. Tsukita, H. Kanoh, S. Nakayama, H. Kashihara, T. Mizuno, H. Tanaka, T. Matsui, Y. Goto, A. Komatsubara, et al. 2021. A microtubule-LUZP1 association around tight junction promotes epithelial cell apical constriction. *EMBO J.* 40:e104712. <https://doi.org/10.15252/emj.2020104712>
- You, Y., E.J. Richer, T. Huang, and S.L. Brody. 2002. Growth and differentiation of mouse tracheal epithelial cells: selection of a proliferative population. *Am. J. Physiol. Lung Cell. Mol. Physiol.* 283:L1315–L1321. <https://doi.org/10.1152/ajplung.00169.2002>
- Yukawa, M., M. Okazaki, Y. Teratani, K. Furuta, and T. Toda. 2019. Kinesin-6 Klp9 plays motor-dependent and -independent roles in collaboration with Kinesin-5 Cut7 and the microtubule crosslinker Ase1 in fission yeast. *Sci. Rep.* 9:7336. <https://doi.org/10.1038/s41598-019-43774-7>
- Zepp, J.A., and E.E. Morrisey. 2019. Cellular crosstalk in the development and regeneration of the respiratory system. *Nat. Rev. Mol. Cell Biol.* 20:551–566. <https://doi.org/10.1038/s41580-019-0141-3>

## Supplemental material

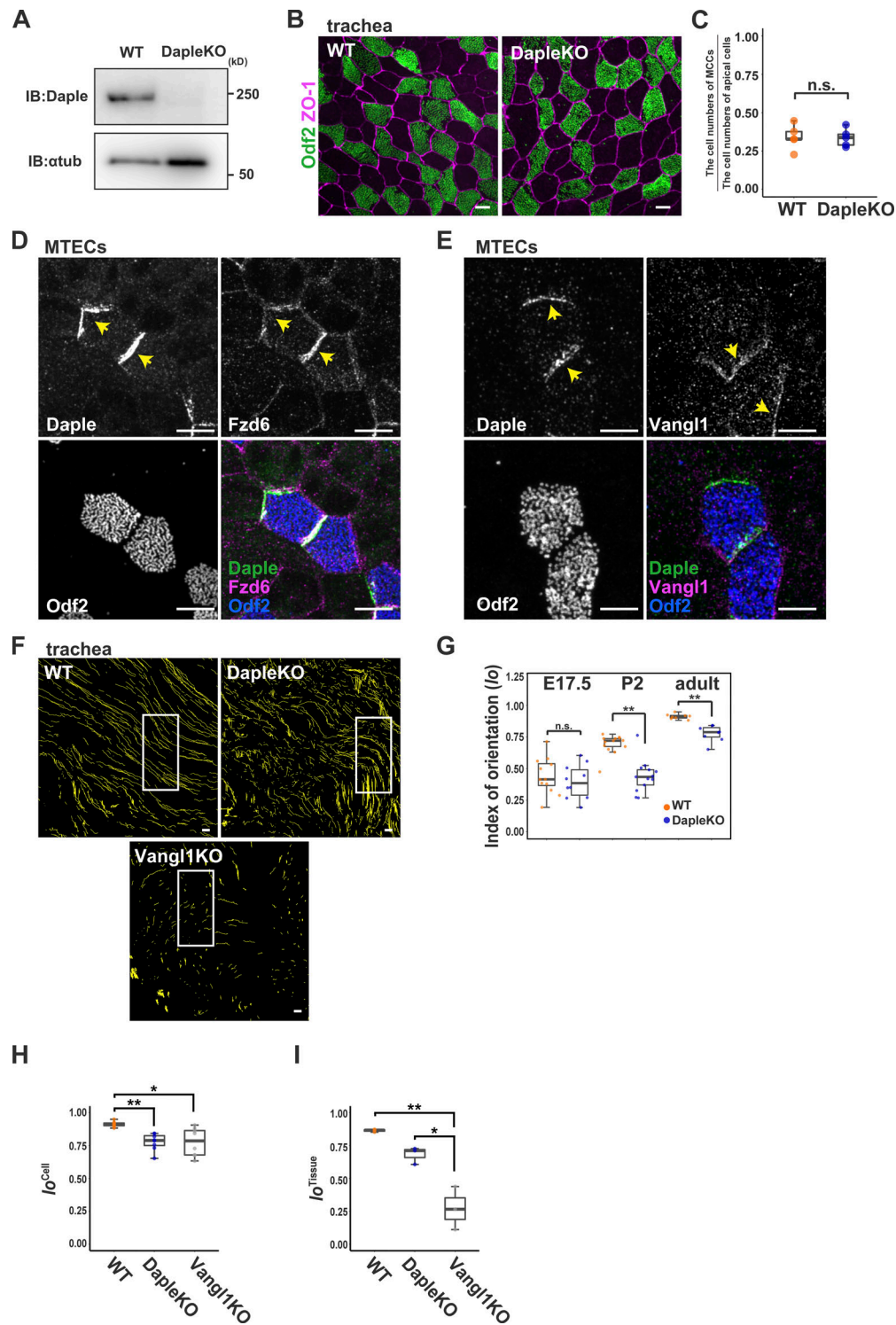


Figure S1. **The phenotype of tracheal MCCs in Daple-KO mice.** (A) Analysis of Daple expression using immunoblotting (IB) in WT and Daple-KO MTECs grown at the ALI for 12 d;  $\alpha$ -tubulin ( $\alpha$ tub) was used as a loading control. (B) Representative images of Odf2 and ZO-1 in WT and Daple-KO tracheas. (C) Analyses of the ratios of total numbers of MCCs against total numbers of apical cells in WT and Daple-KO tracheas ( $n = 5$ ). Two-tailed Mann-Whitney  $U$  test; n.s.,  $P \geq 0.05$ . (D and E) Immunofluorescence images of Daple, Fzd6, and Odf2 (D) or for Daple, Vangl1, and Odf2 (E) in the MCCs of MTECs grown at the ALI for 12 d. Arrows indicate the localization of Daple, Fzd6, and Vangl1. The Odf2 signal (blue) was used as a marker of MCCs. (F) Analysis of mucociliary transport in WT, Daple-KO, and Vangl1-KO adult tracheas using live imaging of fluorescent beads. High-magnification images of the boxed regions are shown in Fig. 1 B. (G) Statistical analyses of  $I_o$  of BBs at the cell level in WT and Daple-KO tracheas at different developmental stages of E17.5, P2, and adult mice ( $n = 8$ –13 cells). Representative images are shown in Fig. 1 G. Two-tailed Mann-Whitney  $U$  test; \*\*,  $P < 0.01$ ; n.s.,  $P \geq 0.05$ . (H and I) Statistical analyses of  $I_o$  values of BBs at the cell level (H;  $n = 8$  cells) and tissue level (I;  $n = 3$  tracheas) in WT, Daple-KO, and Vangl1-KO tracheas. Representative images are shown in Fig. 2 B. Statistical differences were analyzed using two-tailed Mann-Whitney  $U$  tests (H) or Kruskal-Wallis tests with Steel-Dwass multiple-comparison tests (I). \*,  $P < 0.05$ ; \*\*,  $P < 0.01$ . Scale bars represent 5  $\mu$ m in B, D, and E and 10  $\mu$ m in F.



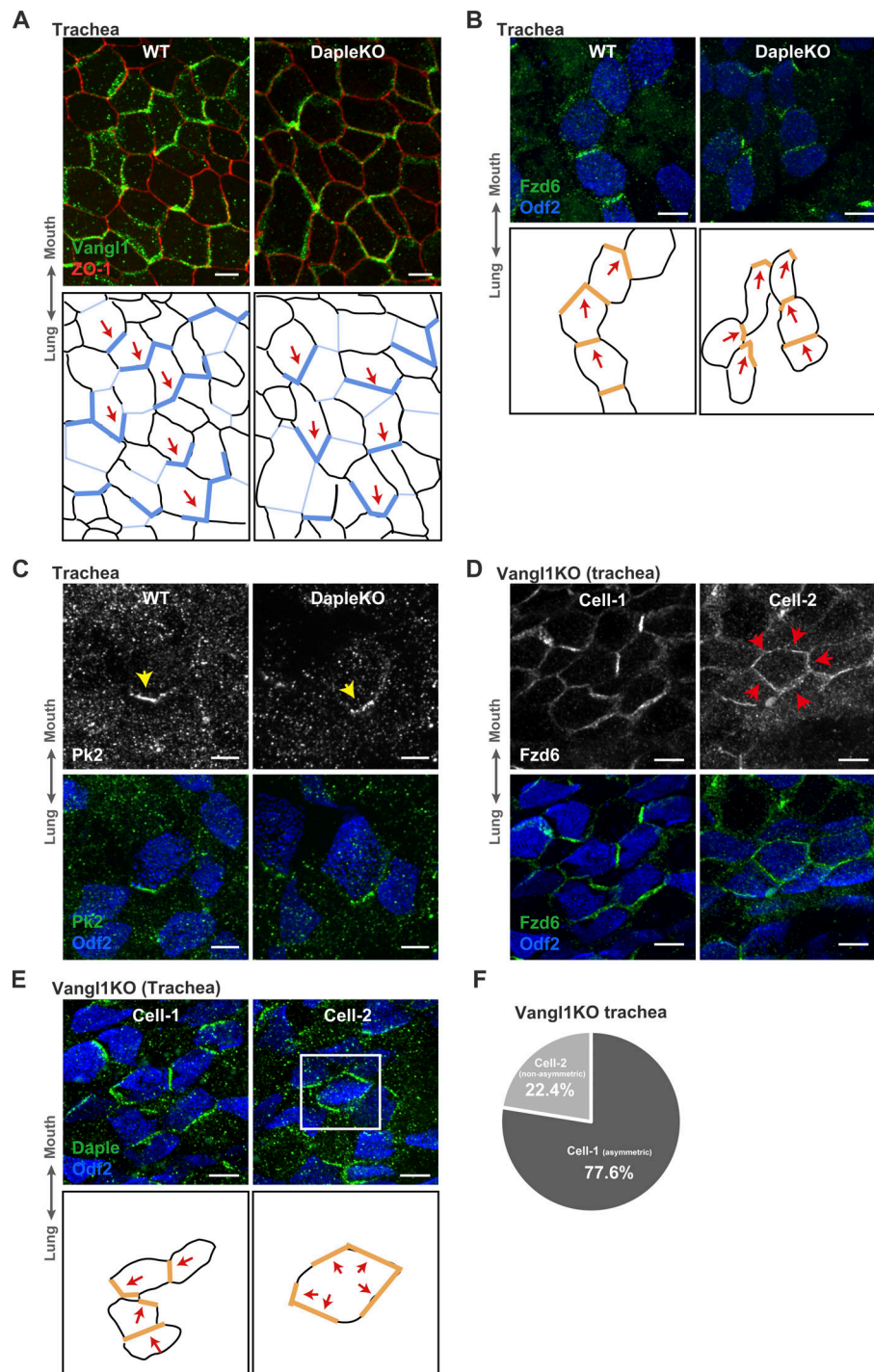


Figure S2. **Daple is a downstream factor of PCP signaling in tracheal MCCs.** (A) Representative immunofluorescence images of Vangl1 (green) and ZO-1 (red) in tracheas of WT and Daple-KO adult mice (upper panels) and schematic illustrations of Vangl1 localization (blue; lower panels). These images correspond to the immunofluorescence images shown in Fig. 2 D. Red arrows display Vangl1 localization in tracheal MCCs. (B) Representative immunofluorescence images of Fzd6 (green) and Odf2 (blue) in tracheas of WT and Daple-KO adult mice (upper panels) and schematic illustrations of Fzd6 localization in MCCs (orange; lower panels). These images correspond to the immunofluorescence images shown in Fig. 1 E. Red arrows show Fzd6 localization in tracheal MCCs. (C) Representative immunofluorescence images of Pk2 (green) and Odf2 (blue) in tracheas of WT and Daple-KO adult mice. Yellow arrows indicate the localization of Pk2 in tracheal MCCs. (D) Representative immunofluorescence images of Fzd6 (green) and Odf2 (blue) in tracheas of Vangl1-KO adult mice. Vangl1-KO MCCs are divided into two types: cell-1 (Fzd6 asymmetrical) and cell-2 (Fzd6 symmetrical). Red arrows indicate the localization of Fzd6 at the AJC in tracheal MCCs. (E) Representative immunofluorescence images of Daple (green) and Odf2 (blue) in tracheas of Vangl1-KO adult mice (lower panels). Schematic illustrations of Daple localization in MCCs (orange; lower panels). Vangl1-KO MCCs were divided into two types: cell-1 (Daple asymmetrical) and cell-2 (Daple symmetrical). These images correspond to the immunofluorescence images shown in Fig. 1 F. (F) Ratio of cell-1 (Fzd6 asymmetrical) and cell-2 (Fzd6 symmetrical) in MCCs of Vangl1-KO mouse tracheas ( $n = 98$  cells). The double arrows indicate the direction of the mounted tracheas in A–E. Scale bars represent 5  $\mu\text{m}$ .

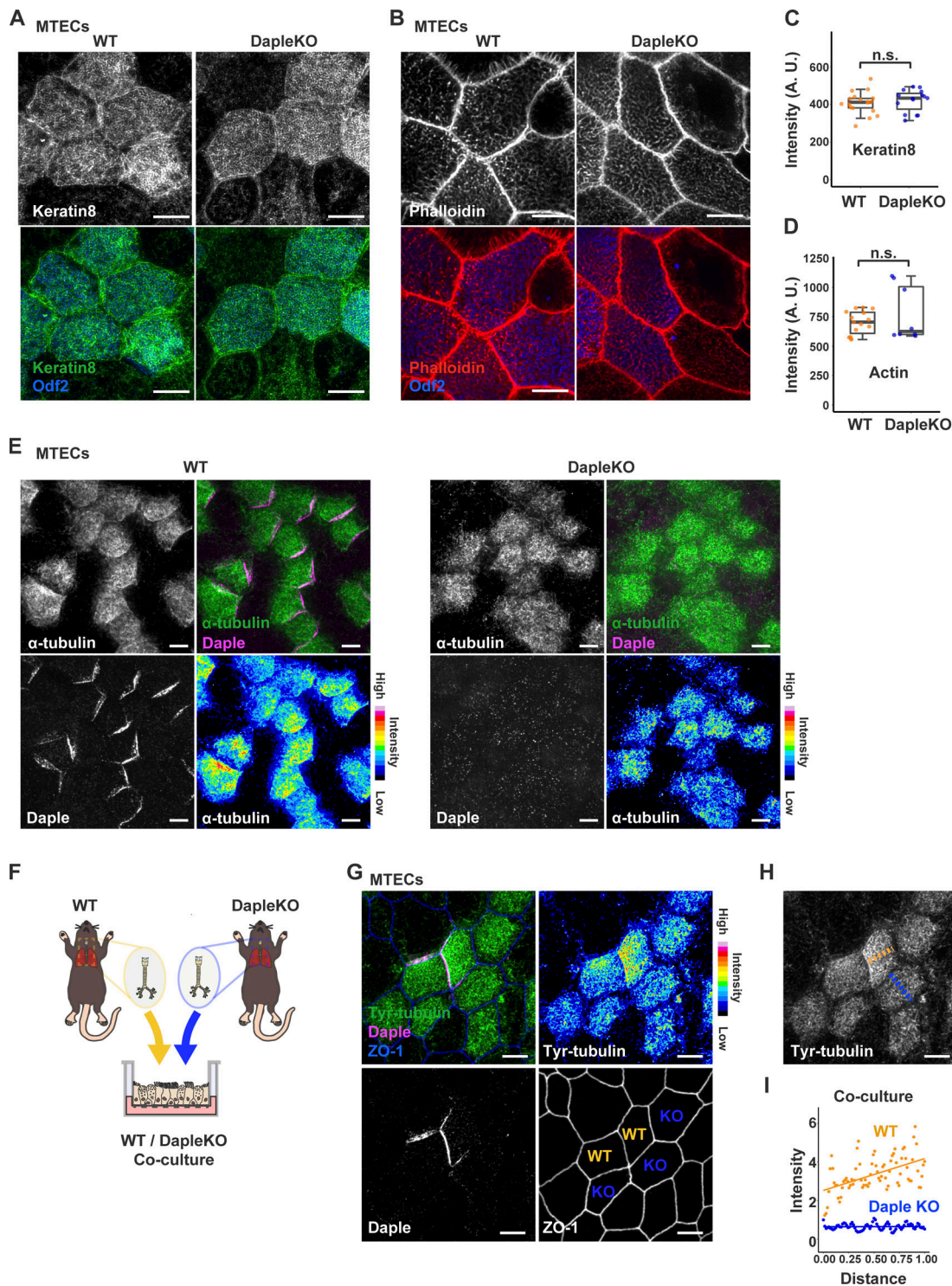


Figure S3. **Daple regulates the planar polarized distribution of MTs in a cell-autonomous manner.** (A) Representative immunofluorescence images of keratin8 (green) and Odf2 (blue) in WT and Daple-KO MTECs grown at the ALI for 12–14 d. The Odf2 signal indicates MCCs. (B) Representative immunofluorescence images of actin (red) and Odf2 (blue) in WT and Daple-KO MTECs grown on the ALI for 12–14 d. The Odf2 signal indicates MCCs. (C and D) Statistical analyses of keratin8 (C) and actin (D) expression in MCCs of WT and Daple-KO tracheas ( $n = 8$ –18 cells). Significant differences were evaluated using two-tailed Mann-Whitney  $U$  tests; n.s.,  $P \geq 0.05$ . (E) Representative images of  $\alpha$ -tubulin (green) and Daple (magenta) in WT and Daple-KO MTECs grown at the ALI for 12–14 d. The Odf2 signal indicates MCCs. The intensity of the  $\alpha$ -tubulin signal is represented by the color map, in which red indicates high intensity and blue indicates low intensity. (F) Schematic illustration of the co-culture method of MTECs prepared from the tracheas of WT and Daple-KO mice. (G) Representative immunofluorescence images of Daple (magenta), ZO-1 (blue), and tyrosinated tubulin (green) in co-cultured MTECs of WT (orange) and Daple-KO (blue) cells grown at the ALI for 12 d. The intensity of the tyrosinated tubulin signal is illustrated by the color map (red indicates high intensity; blue indicates low intensity). Tyr-tubulin, tyrosinated tubulin. (H and I) Immunofluorescence image (H) and intensity profiles for Tyr-tubulin (I) in MCCs of WT and Daple-KO co-cultured MTECs. Scale bars represent 5  $\mu$ m. A.U., arbitrary units.

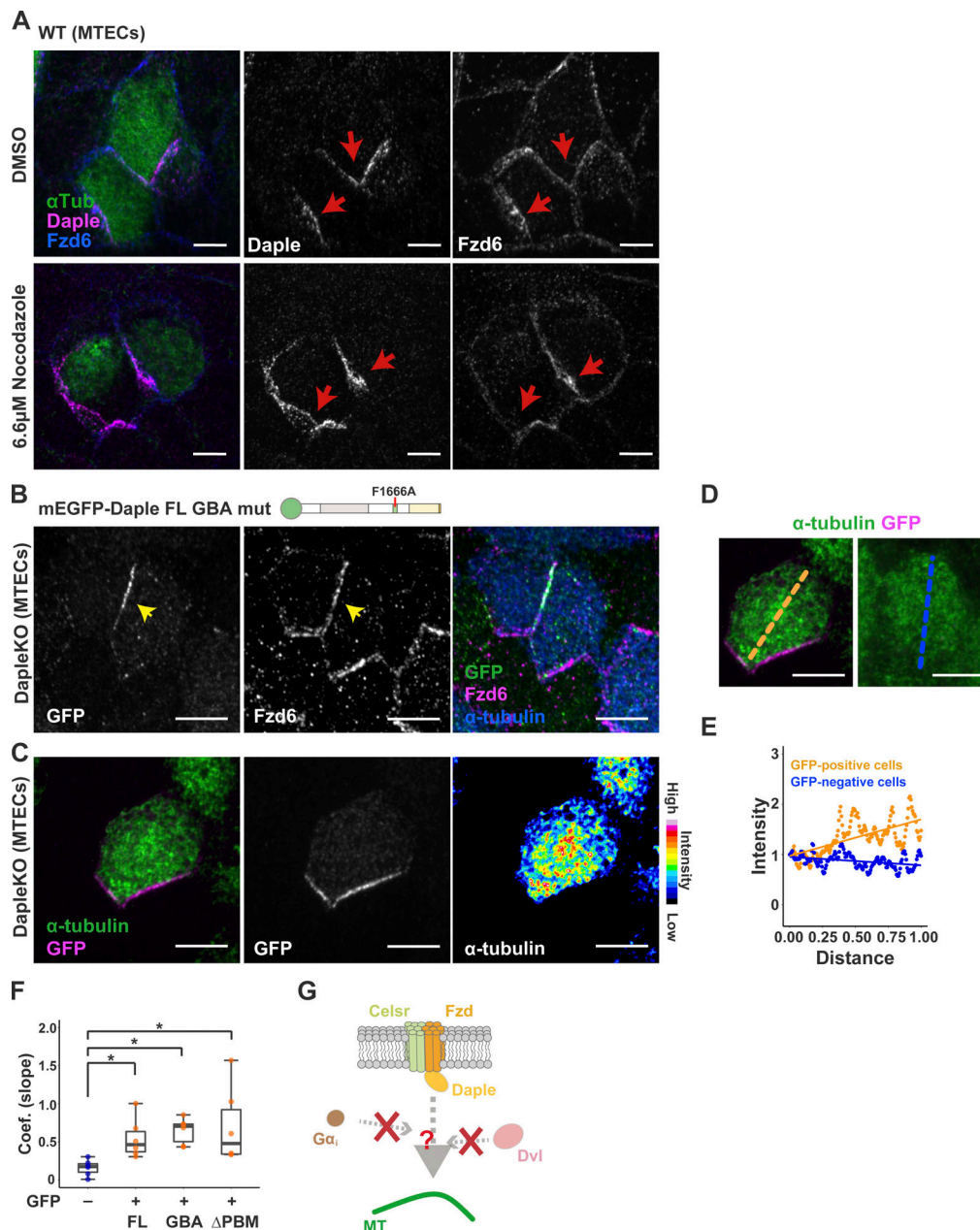
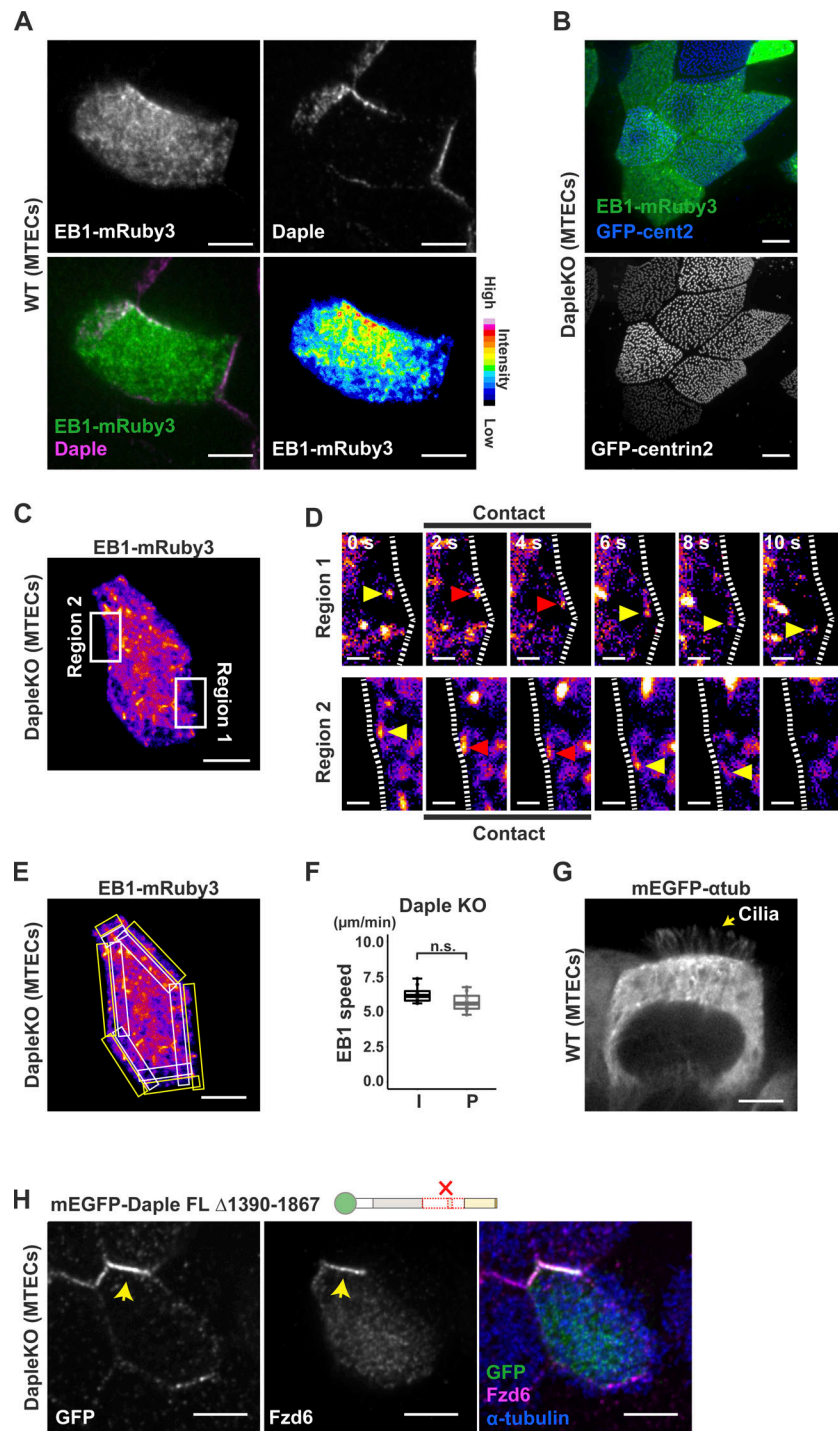


Figure S4. **The  $G\alpha_i$  interactive domain is not required for Daple-mediated MT organization.** (A) Immunofluorescence images of  $\alpha$ -tubulin and Daple in WT MTECs treated with DMSO and 6.6  $\mu$ M nocodazole for 2 h. Red arrows indicate the localization of Daple and Fzd6 in tracheal MCCs. (B) Representative immunofluorescence images of the mEGFP-Daple FL GBA motif mutant (GBA mut; green), Fzd6 (magenta), and  $\alpha$ -tubulin (blue) in Daple-KO MTECs. The mEGFP-Daple FL GBA motif mutant (GBA mut) was expressed using a lentivirus system. Yellow arrows indicate mEGFP-Daple FL (GBA mut) and Fzd6 localization in tracheal MCCs. (C) Representative images of mEGFP-Daple FL (GBA mut; magenta) and  $\alpha$ -tubulin (green) in Daple-KO MTECs expressing mEGFP-Daple FL (GBA mut). The intensity of the  $\alpha$ -tubulin signal is represented by the color map (red indicates high intensity; blue indicates low intensity). (D and E) Intensity profiles of  $\alpha$ -tubulin in mEGFP-Daple FL (GBA mut)-positive MCCs (orange) and -negative MCCs (blue) in Daple-KO MTECs. (F) Statistical analysis of the slope coefficient (Coef.) acquired from the  $\alpha$ -tubulin intensity profiles in mEGFP-Daple FL-, mEGFP-Daple FL (GBA mut)-, and mEGFP-Daple FL  $\Delta$ PBM-expressing MCCs (orange) and Daple-KO MCCs ( $n = 6$  cells). Significant differences were analyzed using Kruskal-Wallis tests with Steel-Dwass multiple-comparison tests. \*,  $P < 0.05$ . (G) Schematic illustration of the proposed mechanism for MT accumulation specifically at the Fzd side of the AJC in a  $G\alpha_i$ - and Dvl-independent manner through Daple. Scale bars represent 5  $\mu$ m.



**Figure S5. MT dynamics at the AJC in WT and Daple-KO tracheal MCCs.** (A) Representative immunofluorescence images of EB1-mRuby3 (green) and Daple (magenta) in GFP-centrin2-positive WT MTECs expressing EB1-mRuby3 using a lentivirus system. The EB1-mRuby3 signal intensity is represented by the color map. (B) Representative images of EB1-mRuby3 (green) and centrin2 (blue) in Daple-KO GFP-centrin2-positive MTECs expressing EB1-mRuby3 using a lentivirus system. (C) Representative images of EB1-mRuby3 in Daple-KO GFP-centrin2-positive MTECs expressing EB1-mRuby3 using a lentivirus system. The areas (regions 1 and 2) were arbitrarily selected on the opposite sides of the AJC. (D) Time-lapse images for EB1-mRuby3 in regions 1 and 2 of the AJC in MCCs of GFP-centrin2-positive Daple-KO MTECs expressing EB1-mRuby3 using a lentivirus system. These images were taken in the boxed regions of C. Red arrowheads indicate the EB1 comets contacting the AJC. Yellow arrowheads indicate the EB1 comets that did not contact the cell membrane. (E) Representative images of EB1-mRuby3 in Daple-KO GFP-centrin2-positive MTECs expressing EB1-mRuby3 using a lentivirus system in which the I and P regions of the AJCs are shown. (F) Speed of EB1 at the I and P regions in MCCs of Daple-KO MTECs expressing EB1-mRuby3 using a lentivirus system ( $n = 8$  cells). Significant differences were evaluated using two-tailed Mann-Whitney  $U$  tests; n.s.,  $P \geq 0.05$ . (G) The vertical plane image of mEGFP- $\alpha$ -tubulin in WT MTECs expressing mEGFP- $\alpha$ -tubulin using a lentivirus system. The arrow indicates cilia. (H) Representative images of mEGFP-Daple FL  $\Delta 1390$ -1867 (green), Fzd6 (magenta), and  $\alpha$ -tubulin in Daple-KO MTECs expressing mEGFP-Daple FL  $\Delta 1390$ -1867 using a lentivirus system. Arrows indicate the localization of mEGFP-Daple FL  $\Delta 1390$ -1867 and Fzd6 in tracheal MCCs. Scale bars represent 5  $\mu\text{m}$  in A-C and E-H and 1  $\mu\text{m}$  in D.

Video 1. **Live imaging of the fluorescent beads in mucociliary transport in isolated adult tracheas.** Analysis of mucociliary transport in isolated WT, Daple-KO, and Vangl1-KO tracheas. The images were acquired at 25-ms intervals. The bead position at each time point is connected in yellow.

Video 2. **Super-resolution imaging of  $\alpha$ -tubulin in MCCs.** Super-resolution images for  $\alpha$ -tubulin are displayed at different z-slices in WT MCCs of MTECs grown on ALI for 12–14 d. Frame rate is 0.5  $\mu$ m z-steps.

Video 3. **UHVEMT imaging of apical MTs in WT and Daple-KO MCCs.** Representative UHVEMT images in which the MTs are reconstituted in 3D (green) in MCCs in WT and Daple-KO adult tracheas. The original images were taken at 25,000 $\times$  magnification from  $-60^\circ$  to  $+66^\circ$  at  $2^\circ$  intervals around a single-tilt axis.

Video 4. **Live imaging of EB1-mRuby3 in WT MCCs.** Live imaging showing the dynamics of EB1-mRuby3 at the Fzd side and the other side of the AJC in WT MCCs of MTECs (Fig. 6 C). The yellow arrowhead indicates the EB1 comet. The images were acquired at 2-s intervals.

Video 5. **Live imaging of EB1-mRuby3 in Daple-KO MCCs.** Live imaging showing the dynamics of EB1-mRuby3 at regions 1 and 2 of the AJC in Daple-KO MCCs of MTECs. The yellow arrowhead indicates the EB1 comet. The images were acquired at 2-s intervals.

Video 6. **Live imaging of MTs in MCCs of WT and Daple-KO MTECs.** Live imaging of mEGFP- $\alpha$ -tubulin showing the dynamics of MTs in MCCs of WT and Daple-KO MTECs. The images were acquired at 2-s intervals.

Video 7. **Live imaging of a single Daple molecule.** Live imaging of mEGFP-Daple FL showing the single-molecule behavior of Daple FL along MTs. The images were acquired at 100-ms intervals.

Video 8. **UHVEMT imaging of MT bundling in MCCs of WT tracheas.** Representative UHVEMT images in which the MTs were reconstituted in 3D (green) in MCCs to show bundling of MTs in WT adult mouse tracheas. The original images were taken at 25,000 $\times$  magnification from  $-60^\circ$  to  $+66^\circ$  at  $2^\circ$  intervals around a single-tilt axis.